DEPARTMENT OF TRANSPORTATION

Sensing for HOV/HOT Lanes Enforcement

Nikolaos Papanikolopoulos, Principal Investigator
Department of Computer Science
University of Minnesota

FEBRUARY 2017

Research Project
Final Report 2017-05

To request this document in an alternative format, such as braille or large print, call 651-366-4718 or 1-800-657-3774 (Greater Minnesota) or email your request to ADArequest.dot@state.mn.us. Please request at least one week in advance.

Technical Report Documentation Page

1. Report No.	2.	3. Recipients Accession No.	
MN/RC 2017-05			
4. Title and Subtitle Sensing for HOV/HOT Lanes Enforcement		5. Report Date February 2017	
		6.	
7. Author(s) Ted Morris, Vassilios Morellas, Dario Canelon-Suarez, Nikolaos Papanikolopoulos		8. Performing Organization Report No.	
9. Performing Organization Name and Address Department of Computer Science University of Minnesota 500 Pillsbury Drive S.E. Minneapolis, MN 55455		10. Project/Task/Work Unit No. CTS #2014051	
		11. Contract (C) or Grant (G) No. (c) 99008 (wo) 91	
12. Sponsoring Organization Name and Address Minnesota Department of Transportation Research Services & Library 395 John Ireland Boulevard, MS 330 St. Paul, MN 55155		13. Type of Report and Period Covered Final Report	
		14. Sponsoring Agency Code	
15. Supplementary Notes http://mndot.gov/research/reports/2017/201705.pdf			

16. Abstract (Limit: 250 words)

The use and creation of combined high-occupancy vehicle/high-occupancy toll (HOV/HOT Lanes) have become more common in urban areas since all types of road users can take advantage of the lane either as a high-occupancy vehicle or opting in to pay a congestion adjusted free. However, to maintain working integrity of the lanes for all users, stepped enforcement to discourage cheating has been needed as more lanes are added. This study evaluated the capability of a novel image sensor device to automate detection of in-vehicle occupants to flag law enforcement of HOV/HOT lane violators. The sensor device synchronously captures three co-registered images, one in the visible spectrum and two others in the infrared bands. The key idea is that the infrared bands can enhance correct occupancy detection through known phenomenological spectral properties of objects and humans residing inside the vehicle. Several experiments were conducted to determine this capability across varied conditions and scenarios to assess detection segmentation algorithms of vehicle passengers and drivers. Although occupancy detection through vehicle glass could be achieved in many cases, improvements must be made to such a detection system to increase robustness and reliability as a law enforcement tool. These improvements were guided by the experimental results, as well as suggested methods for deployment if this or similar technologies were to be deployed in the future.

17. Document Analysis/Descriptors	18. Availability Statement		
vehicle occupancy, high occupancy vehicle lanes, high occupancy toll lanes, sensors, intelligent transportation systems, real time information	No restrictions. Document available from: National Technical Information Services, Alexandria, Virginia 22312		
19. Security Class (this report) Unclassified	20. Security Class (this page) Unclassified	21. No. of Pages 64	22. Price

SENSING FOR HOV/HOT LANES ENFORCEMENT

FINAL REPORT

Prepared by:

Ted Morris
Vassilios Morellas
Dario Canelon-Suarez
Nikolaos Papanikolopoulos
Department of Computer Science
University of Minnesota

FEBRUARY 2017

Published by:

Minnesota Department of Transportation
Research Services & Library
395 John Ireland Boulevard, MS 330
St. Paul, Minnesota 55155-1899

ACKNOWLEDGEMENTS

The authors would like to acknowledge individuals and organizations that made this research possible. The study was funded by the Minnesota Department of Transportation (MnDOT). There are several individuals from MnDOT who through their time, cooperation, and advice, provided invaluable support and guidance for the project: Brian Kary, acting regional transportation management center Engineer and the project technical assistance panel (TAP) lead, and of his regional traffic management center (RTMC) staff for their valuable time and feedback, as well as Jerry Kotzenmacher for providing access initially to the I-394 test facility. The authors also acknowledge the University of Minnesota Center for Transportation Studies for its administrative support. We also thank the University of Minnesota Police and Steve Sanders from University of Minnesota Parking Services for their cooperation in providing our team repeated access to outdoor facilities for running the myriad of experiments for the study.

TABLE OF CONTENTS

LIST OF FIGURES

LIST OF TABLES

EXECUTIVE SUMMARY

The utilization of high-occupancy vehicle/high-occupancy toll lane facilities continues to grow in major metropolitan areas since they provide a viable alternative to more efficient lane utilization and increasing person-per-lane throughput. This is especially true within the Minneapolis-St. Paul metropolitan area where more such lanes have come online or are in the planning phases. For such facilities to operate most effectively all users must comply with the law. Such enforcement is a non-trivial task to carry out strictly through manual intervention, especially as HOT/HOV lane facilities continue to expand.

The original goal of this project was to evaluate detection capabilities of a sophisticated commercial image sensor for automating the process of detecting in-vehicle passenger occupants driving within the HOV/HOT lane facilities as a tool to check user compliance and law enforcement activities. The sensor synchronously captures three spectral band images: one in the visible band, and two others within the near, short wave infrared (SWIR) range. However, early on in the project it became clear that penetrating the windshield turned out to be a far more complex, yet fundamental, problem that must be understood with the operational principles of the sensor before any such system can be fully deployed for the intended task. In particular, with today's vehicle windshields and side window glass compositions, a key challenge is understanding and specifying active illumination systems that both supply sufficient power at required spectral ranges while imposing minimal risk of eye safety hazard to motorists.

The primary objective of this study was to therefore conduct several controlled experiments with the sensor to understand limitations of detection and supporting algorithms to process the data for efficient segmentation and detection. One set of experiments consisted of laboratory experiments in controlled ambient conditions (no infrared range light could influence detection experiments) utilizing several original equipment manufacturer (OEM) vehicle glass samples from 'typical' passenger vehicles. The results from these experiments analyzed the effect of modifying active illumination with supplemental and carefully controlled coherent sources and determined that indeed detection was sensitive to such additions.

A second set of outdoor experiments further explored vehicle positioning and ambient environmental lighting conditions across different vehicles to carry out a similar assessment. Between these sets of experiments, inferred active illumination levels that may be required for effective detection using this sensor were estimated. A discussion of eye safety hazards through examples of potential coherent active illuminators is provided for the Honeywell tri-band infrared imaging sensor (TBI). The presented analysis can be applied similarly to other near infrared (NIR) image-sensor-based detection systems for HOV/HOT lane monitoring.

The general conclusion is that penetration is indeed possible with the sensing technology through supporting infrastructure such as the active illumination to allow robust performance. This study utilized illumination technology that was very low cost, although scaling it to the inferred level after experimentation may not be a practical alternative.

CHAPTER 1: INTRODUCTION

Combining high-occupancy vehicle (HOV) and high-occupancy toll (HOT) lanes are becoming quite popular since they can provide innovative solutions to congestion and traffic safety [1]-[3]. Before the 1998 TEA 21 provisions to allow legal authority of such lanes, HOV-only lanes mostly went underutilized. With a combined HOV/HOT lane, a high occupancy toll is a fee that is applied to vehicles with only one occupant that use lanes intended for vehicles with more than one occupant. The goal is to achieve the same person throughput as regular lanes but without the congestion, by fluctuating the fee in real-time from an estimate of the traffic volume in the lane. There may also be a safety benefit for reducing crashes over HOV lanes by smoothing the traffic flow and speeds. HOV/HOT lanes also discourage illegal solo drivers from cutting in and out of the dedicated lane, since they can opt-in by paying the fee [3]. Most at grade HOV/HOT lanes can charge the fees without any human intervention such as toll booths with human cashiers, instead relying on automated electronic means placed within entrance and exit zone areas, which for example are demarcated by painted lines between the HOV/HOT lane and the adjacent regular traffic lanes. In some HOT/HOV lane designs to further reduce implementation costs, the non-entry portions of the lanes are isolated with plastic cones or pavement striping accompanied with no-entrance notification signage, instead of physical barriers or road separation. Such automated charging systems use electronic devices such as wireless transponders tags, or Automatic License Plate Recognition (ALPR) devices. Numerous major corporations have been involved in the design of these systems. For example, Motorola Inc. has developed a system for ALPR that uses a sensor along with a Back Office System Server (BOSS) and AirMobile integration. Elsag North America, an Israeli manufacturer, makes several products in the area of ALPR.

Enforcement is also a necessary part of HOT/HOV lane operations to catch violators to maintain the operational integrity of the facilities. This is a manually intensive effort and can also create a traffic safety hazard. Typically, the Law Enforcement officer first monitors HOT/HOV lane entrance points to wait for vehicles by driving within, or next to, the HOV/HOT lanes where a transponder signal is not received from the passing or entering vehicle in the lane, and then catches up and drives alongside the vehicle to pear into the windows to check for passengers [4]. Video cameras have also been used to monitor locations remotely from a fixed vantage point but the composition of vehicle windshields and side windows can make these observations very challenging depending on environment lighting conditions. In these instances the officer must revert back to the aforementioned strategy to follow the vehicle to confirm passenger occupancy [5].

Since the conversion of the I-394 HOV facilities into HOV/HOT lane in the Twin Cities, more HOV/HOT lane conversions and additions are occurring, for example on Interstate 35W south and, very recently, Interstate 35E north of Saint Paul. This has created the necessity to expand the aforementioned manual monitoring and enforcement efforts using peace officers [6]. Attempting to catch every violator is impractical and, as mentioned previously, can also create a safety hazard for Law Enforcement officers. Thus the motivation for this research project to instead investigate a computer vision based fixed roadside sensor to automate passenger detection to aid enforcement efforts.

1.1 PROJECT RESEARCH SCOPE AND OBJECTIVES

The main objective of this research was to assess the capability of the Honeywell Tri Band Infrared (TBI) sensor to penetrate vehicle glass to 'see' and discriminate human occupants. This sensor was originally used to automate false intrusion detection at high security entrance gates. Originally, the system was to be deployed at an HOV/HOT lane location to evaluate the performance of the sensor. However, through initial experimental field testing early on in the study, the interrelation between infrared range illumination, exposure, and the fundamental tenant of its operational principle proved to be significantly more complex than could originally be anticipated, which could best be addressed and understood through extensive controlled experimentation. The efforts therefore focused on several controlled indoor and outdoor experiments to understand limitations and capabilities of the sensor in the context of future HOV/HOT lane deployment scenarios. The results also provide a tangible framework for evaluating similar detection systems that may be considered for future deployments.

1.2 REPORT ORGANIZATION

The report is organized as follows. Chapter 2 provides background of other relevant work in computer vision circles for detecting human occupancy. Chapter 3 provides a brief synopsis the detector principle of operation and processing methodology to enable synchronous real-time visible tri-band image acquisition and human subject detection. Chapter 4 summarizes laboratory controlled experimental results to evaluate artificial IR band illumination and computer vision segmentation approaches. Chapter 5 then summarizes outdoor experiments with controlled relative vehicle-sensor positioning and environmental conditions. Chapter 6 provides an overview of eye safety risk for active illumination. General conclusions and recommendations are presented in Chapter 7.

CHAPTER 2: BACKGROUND

There have been numerous efforts that utilized image sensors to detect vehicle occupants. Penetrating vehicle glass to "see" the occupants using strictly visible range imaging is a very challenging problem—for example due to reflective glare or dark conditions. Furthermore, other sensor types whose performance do not depend on lighting conditions such as Microwave and UWB Radar, generally do not have the sampling bandwidth, or capability to penetrate tinted vehicle windows [7]. Heat sensing infrared image sensors have also been considered to detect the human subject foot print but in-cabin heating thwarts the ability to isolate the heat signatures of human passengers within the image [8]. Furthermore, in order to reduce solar glare and in-cabin heat loads, many of today's windshields and side windows have characteristics which are designed to block out near infrared (NIR) band light energy. Nevertheless, recent research and development have focused on imaging within the Infrared range since potentially they provide robust detection in varied environmental conditions compared to visible band cameras [9], [10]. The infrared image sensing, even when supplemented with high power illumination, cannot distract drivers since it is not in the visible range. Such image sensors are also commercially widely available, thus representing a potentially cost effective and low maintenance solution. Many of the commercially available IR image sensors are capable of acquiring images at very high framerates—a requirement for capturing data from vehicles moving at freeway speeds.

Some researchers have focused on NIR Imaging with a response band just beyond the visible range with the rational that a modest fraction of light energy should still be able to penetrate within the spectral range of a 'transition zone' from the visible to IR spectrum [4], [11]-[14]. For example researchers in [12] tuned the response at the desired band by adding a special notch IR bandpass filter within 800 to 850nm. A commercial IR Xenon Flash illuminator was also integrated to provide active IR illumination with an equivalent total power output of 10KWatts generated within 100 microseconds, which was found to be adequate for the deployed positions of the sensor (on the road edge of the HOV lane of oncoming vehicles). The detection was based on first identifying the vehicle window by training a Histogram Of Gradiant (HOG) detector to isolate a region of interest (ROI) encompassing the vehicle window. Then, for true-positive window identifications, the edge features of the window pain is identified to further isolate the window feature. The passenger detection and counting was then achieved by training the well-known HAAR cascade face detection algorithm to detect human face objects within the windshield boundary. They tested a dual sensor configuration for stereo reconstruction to further discriminate passengers by estimating the detected face blob's 3D location [7]. Their results indicated an overall occupancy detection accuracy greater than 80% for the vehicle windows detected (85%). Most of the occupancy detection errors were due to false positive face detection. Their detection system was least successful in bright sunlight.

Hao et al. [11] investigated a NIR sensing system utilizing a notch 40nm wide band pass NIR filter, centered on 820nm to enhance human occupancy detection to either aid the enforcement officer or as a pre-cursor for automated identification. They proposed projecting high power IR illumination within this band through the side windows to minimize the probability of direct eye exposure by the occupants. Interestingly, they present windshield spectral transmissivity characteristics showing a secondary

infrared peak between 1400 and 1700nm, which was about seventy-five percent of the transmissivity of the visible band peak. This secondary peak corresponds to upper IR band of the TBI sensor in the study. Note that limited experimental results were provided in their work.

Within recent patent literature, other groups have used the invariant skin absorption properties within the 1400nm to 1700nm shortwave near infrared (SWIR) range for human face detection. Dalal et. al [15] proposed a processing of SWIR windshield images captured real-time through a bandpass filter with the aforementioned range. Note this is analogous to the Honeywell TBI SWIR upper band image filtered above 1400 nanometers. A cumulative gray scale intensity histogram was computed across a candidate region of interest (ROI) representing the windshield, followed by thresholding to segment out an intensity range of darker pixels which should contain human faces. HOG feature patches are then used on the remaining images to associated face and non-face objects. Zhang et al. [14] propose a Fabry-perot honeycomb filter and lens to project a multi-spectral band images upon a single IR range image sensor. The segmentation of human skin (as well as other object surfaces) is achieved by using principle component analysis (PCA) through singular value decomposition (SVD) across the ensemble of spectral band images to classify human skin from other object surfaces. Gray scale difference images are then calculated between each of the spectral band images to differentiate human skin from other inert materials within the vehicle, through binary thresholding and connected component blob regions.

Pavlidis et al. [8], [16] evaluated a dual band SWIR sensor that introduced the principle of operation of the Honeywell TBI sensor, without the visible range imager. Active illumination was used as part of the sensor system with closed loop radiant power control in order to preserve a theoretical signal to noise ratio, using photometric input signals. Passenger counting was evaluated by training a Neural Network with 100 randomly selected sample images taken from a test vehicle traveling at 65 Miles/hour across different environmental conditions, to discriminate between a front seated passenger and the driver, or just the driver. The processing and classification algorithms were 100 percent accurate across all the samples.

Holec et al. compared automated human occupancy detection performance of a dual NIR camera setup with visible band color images [17]. Similar to the TBI sensor, two filters shortwave infrared (SWIR) band filters were used; a short pass filter with a cut-off below 1400 nanometers, and a long pass filter with a cut-off above 1400 nanometers. Each IR filter was mounted over the lens of two NIR sensitive cameras, both of which were responsive to the SWIR spectral band wavelengths between 900 to 1700 nanometers. Image co-registration between the three separate camera images was achieved through optimal search of an affine transform. Machine learning classifiers were developed for the extracted blob feature data. The results indicated that the color information from the visible band images alone could detect the occupants comparable to the SWIR configuration. However, cloudy or darker conditions were not performed for these experiments. There was no active illumination source in their detection system.

A commercial NIR sensor prototype, *dtect,* originally developed and built by Vehicle Occupancy Ltd., of Leicester, U.K., was tested by the California department of transportation [18]. As described within the report, the system bares some similarities to the TBI, though details of its specifications and principle of

operation are lacking. For the testing, the device was installed on a jersey barrier separating the HOV lane, aiming directly at oncoming vehicle windshields, with a laser tripwire installed above an overpass to trigger the *dtect* image acquisition. The detection results were either inconclusive or indicated a very high false-detection rate. However, authors believe that tuning the sensor system configuration—such as illuminator power, exposure settings, as well as the triggered relative positions of the vehicles with respect to the sensor, might have significantly improved occupancy detection results.

To conclude, a body of research has evaluated and explored image sensors which operate in the Near Infrared spectrum for in-vehicle human occupancy detection, with some promising results. It should be noted however that many of the aforementioned studies focused on NIR image sensors which do not operate within the same spectral regions as the TBI. The shorter, near-visible NIR band can easily be thwarted into generating false positive passenger detections by simply replacing a dummy in the passenger seat since the reflected intensity data between human skin and the dummy are similar. In contrast, the principle of operation of the TBI mitigates this problem by exploiting the aforementioned spectral reflectance properties of human skin across different bands across the SWIR region (explained in detail in Chapter CHAPTER 3:). Lastly, most studies propose or utilize high intensity active Infrared range illumination to enhance detection with very little attention given to understand any risk level of eye-safety hazards, which was addressed further in this study. This may be particularly important since many of the active illuminators that were used in the cited studies are either no longer manufactured, or cannot provide the correct light wavelengths needed for imaging sensors with similar specifications to those that were integrated within the Honeywell TBI.

CHAPTER 3: DETECTION METHODOLOGY

The primary principle of utilizing the infrared camera sensors is that the quality of the image signal can be retained during overcast days and nighttime, because the scene can be illuminated with non-visible infrared light. The near-infrared cameras can also provide clear imaging signals even in certain foul weather situations, such as hazy conditions. This is very important for HOV/HOT lane operation, because haze is endemic in certain metropolitan areas (e.g., San Francisco). The focal point of the method is the fusion of the co-registered imaging signals from the lower and upper band cameras (the visible band is also co-registered). The phenomenology of human skin demonstrates an abrupt drop in reflectivity just beyond 1.4 micrometers (1400 nanometers) in the Infrared range, where reflectivity is about 5 times less than the reflectivity within the NIR band (700nm to 1400nm) [8]. This results in the intensification of the occupant face silhouettes and the diminution of the background that facilitates robust segmentation of faces of the vehicle occupants. The general methodology and sensor device description to achieve this is described next.

3.1 TBI PRINCIPLE OF OPERATION

The TBI integrates three separate commercial off-the-shelf image sensors that are mechanically co-registered and aligned to pass through the same lens focal axis: 1) A Pulnix model TM 6702 black and white analog CCD 648x484 image sensor, and 2) two 320x255 25µm pitch Indium Gallium Arsenide (InGaAs) focal plane array (FPA) short wave infrared (SWIR) sensitive image sensors, model #SU320MS-1.7RT, which were originally manufactured in May 2003 from Sensors Unlimited (purchased by UTC Aerospace Systems Inc., New Jersey). The optical sensitivity of the SWIR sensors is from 900nm to 1700nm, with a quantum efficiency greater than 65% from 1000nm to 1600nm). The three image sensors are aligned orthogonally through an assembly of beam splitting, mirror, and IR band pass filters (Figure 3.1). A C-mount 10-100mm zoom lens, with motorized focal length, focus, and iris control (Rainbow S10x10M-II) projects the single scene image from approximately 5º to 30º horizontal field of view. One beam splitter passes the collimated light to the visible spectrum imaging sensor, while a subsequent splitter and filter assembly splits the lower band 900 to 1400nm spectral range, and upper band 1400nm-1700nm spectral range, to the SWIR sensors.

An active IR illuminator device was also integrated with TBI sensor. The device, manufactured by Derwent Systems Ltd. (United Kingdom), reflects IR the output light spectrum above 940nm from a 220W quartz halogen bulb through a Fresnel lens, to project a thirty degree horizontal by fifteen degree vertical elliptical spot.

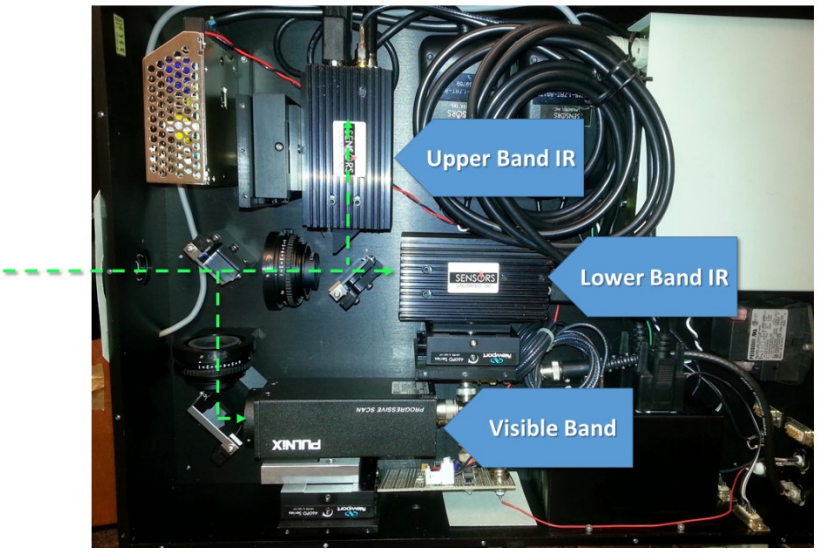

Figure 3.1. Honeywell Tri-band sensor and optics configuration

Like the visible spectrum B&W video sensor, both SWIR sensors provide RS170 compatible analog video signals, although they are inherently digital devices. The TBI sensor does not interface with the converted analog output signals from the SWIR sensors but instead utilizes the camera's EIA422 twelve bit parallel digital interface in order to obtain precise readings of horizontal and vertical synchronization signal clock timings of the captured image. Each sensor output is interfaced to a dedicated PCI frame grabber board; two EIA422 LVD compatible PCI Matrox Corona frame grabbers for the SWIR sensors, and a multi-channel RS170 compatible Matrox Meteor II video frame grabber, for the visible range sensor.

Temporal alignment of the pixel clock timings between SWIR image sensors is achieved through utilization of the External trigger signal (6.01 MHz clock). In this mode, the image sensors will initiate a *single* image scan resulting in very low synchronization varies between two and four pixel clock periods (665 ns). The external TTL trigger pulse is generated through custom analog electronics that detect the start of each frame scan from the visible band camera signal. The SWIR shutter speeds can be set with pre-programmed settings from 0.127 to 16 milliseconds, in power-of-two increments, using RS232 connections to the host data acquisition PC.

3.2 REGISTRATION AND SEGMENTATION

As previously mentioned, human subject detection is facilitated by segmentation of exposed skin from other objects through phenomenological properties of skin reflectance within the two Infrared bands. Specifically, foreground occupant segmentation is achieved by algebraic summation between the two co-registered SWIR lower and upper band images. This requires perfect co-registration between the pairs of images. Early field tests of the sensor revealed that the images were not spatially aligned due to

mechanical misalignment of the internal optics. This confounded extraction of the human subject silhouettes. An initial attempt to physically realign the optics provided a slightly better co-registration but still insufficient for the extraction step. A software solution modeling the misalignment as an affine linear transform was conducted instead to align each given image point $[u, v]^t$ in the one IR image $\boldsymbol{I}$ into the second IR image $\boldsymbol{I}'$ (3.1). Such a model of the co-registration error is reasonable since the projected images retain the same perspective viewpoint. The following process was applied between all three bands.

$$\begin{bmatrix} u' \\ v' \end{bmatrix} = \begin{bmatrix} a_{11} & a_{12} \\ a_{21} & a_{22} \end{bmatrix} \cdot \begin{bmatrix} u \\ v \end{bmatrix} + \begin{bmatrix} t_u \\ t_v \end{bmatrix} \tag{3.1}$$

In order to estimate the 6 unknown affine model parameters, $\{a_{11}, a_{12}, \dots, a_{22}, t_u, t_v\}$ a minimum of three matching image points between the SWIR images must be identified. Because of image signal noise, if a redundant set of good candidate (putative) matching feature points greater than 3 points can be identified across one or more image pairs, then a better estimate of the affine transform model in (1) can be estimated. The solution estimate is then obtained through a Least Squares Maximum Likelihood Estimation.

To determine good candidate image points to match, SURF detection key points and patch descriptors were first calculated for several IR image pairs. The SURF key point algorithm is a computationally efficient, well established method, which is fairly robust to differences in scale, blur artifacts, and slight rotations between similar images [19]. Several such pairs of images (ten pairs) were selected arbitrarily from experiments which collected data from a vehicle parked at four evenly spaced distances between 25 and 130 feet (7.6 and 39.6 meters) from the sensor, to test the robustness of the technique. Putative matches were then extracted based on Euclidian nearest neighbor search of the associated SURF feature descriptors associated with each candidate image point. As shown in Figure 3.2, occasional outlier matches typically occur between the two spectral band images which can significantly reduce the accuracy of the re-alignment model. The RANSAC algorithm was thus employed to fit the affine transform to align the lower band SWIR spectral image (between 900nm and 1400nm) with the upper band SWIR spectral image (between 1400nm and 1700nm). The pixel error for the affine alignment model resulted in a root mean squared error equal to 1.02 pixels, with maximum absolute error of 1.96 pixels.

Single driver subject in-vehicle, 60 ft.

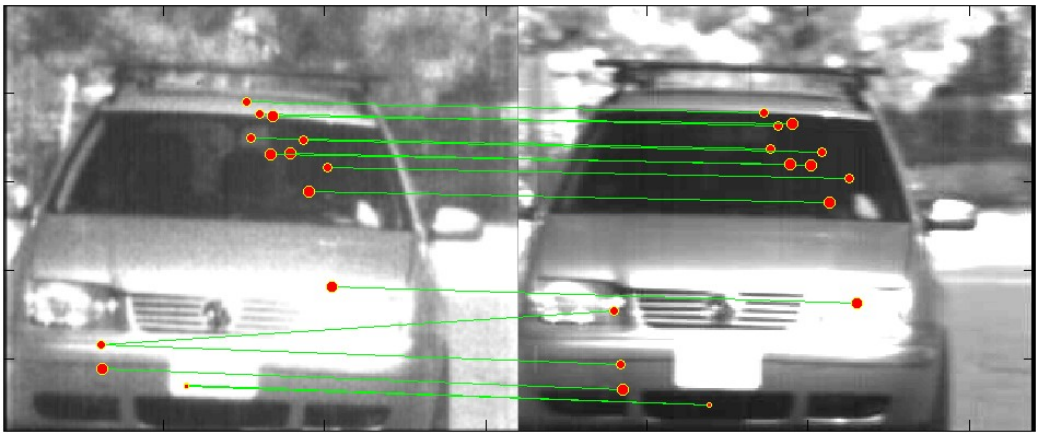

Subject outside vehicle, 100 ft.

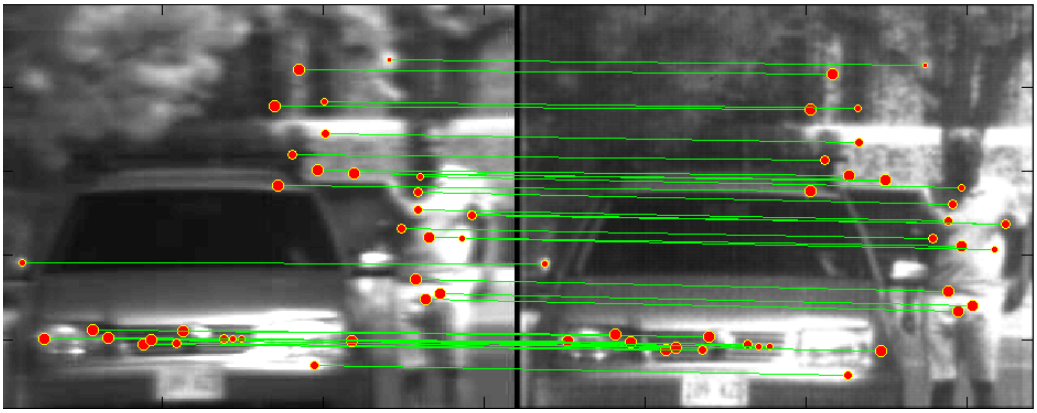

Subject outside vehicle, 130 ft.

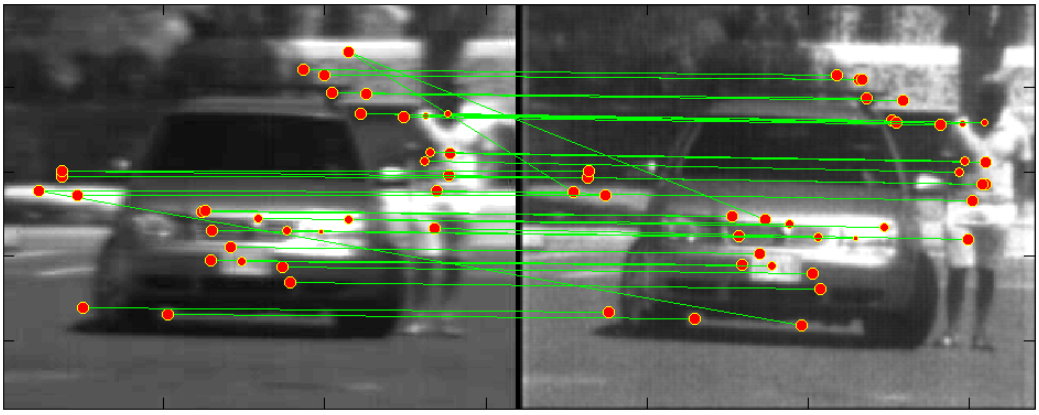

Figure 3.2 Initial putative SURF keypoint candidate matches in *LEFT:* lower band IR (under 1400nm), and *RIGHT:* upper band IR (above 1400nm). The size of the circles indicate stronger match scores between SURF descriptors.

The segmentation step then follows through image arithmetic weighted subtraction between the lower, and upper, IR bands (3.2), producing an intensity difference image that can be thresholded to segment human subjects from other object surfaces through active thresholding of $I(u,v)_D$ and blob formation techniques (Figure 3.3), which described in more detail in subsequent chapters).

$$I(u,v)_D = K_{Lower} \cdot I(u,v)_{Lower} + K_{Upper} \cdot I(u,v)_{Upper} \tag{3.2}$$

Figure 3.3. Human subject segmentation process. UPPER LEFT: Lower band < 1400 nm Image, $I(u,v)_{Lower}$; UPPER RIGHT: Upper band > 1400nm Image, $I(u,v)_{Upper}$, LOWER LEFT: Difference Image, $I(u,v)_D$, LOWER RIGHT: segmentation binary image.

CHAPTER 4: TBI EXPERIMENTAL ASSESSMENT OF VEHICLE GLASS PENETRATION

Initial outdoor field experimentation with the Honeywell TBI sensor revealed limitations of the sensor's capability to penetrate modern vehicle glass. In those experiments, the longitudinal position of oncoming forward facing vehicles were located between 25 and 140 feet from the sensor (Figure 3.2). The experiments were initially designed and conducted to guide deployment constraints on plausible sensor positioning with respect to HOV lanes. One limiting factor that contributed to the experimental results was the TBI illuminator component. This was evident by examining collected data with, and without, the illuminator energized during both, cloudy and sunny conditions. It should be noted that although previous experiments from earlier studies showed superior performance from an earlier prototype [16], the experiments were done almost 15 years ago, and the possibility that vehicle windshield glass optical properties may have changed substantially since then cannot be ignored (the team searched unsuccessfully in local salvage yards to try and find the specific glass used in their experiments). Illumination technology specification details were also not published. To further explore illumination and sensor limitations associated with the TBI with more recent vehicle glass materials, several controlled indoor experiments were conducted. Their descriptions and results are presented below.

4.1 ACTIVE ILLUMINATOR EXPERIMENT DESCRIPTION

Two IR coherent illuminator sources were purchased (OptoEngine, LLC, Midvale, Utah) to increase photonic energy in the TBI SWIR lower band (below 1400 nm) and upper band (above 1400 nm) spectrums. Specifically two 2.5 Watt air cooled continuous wave (CW) diode lasers at 1064±10nm and 1550±10nm were mounted on a machined stacked dual tilt platform, with separate lens and filter holders aligned in front of each laser's exit aperture (fabricated in-house**,** Figure 4.1). Light energy at 1060nm wavelength is reflected by skin tissue, while the wavelength surrounding1550nm is mostly absorbed by skin tissue. Both wavelengths are within the operational spectral range of the TBI SWIR sensors and definitively under, and over, the 1400nm IR band pass filter and splitting optics of the SWIR sensor. Laser interlocked power supplies meeting LSO and University guidelines were used to power the lasers.

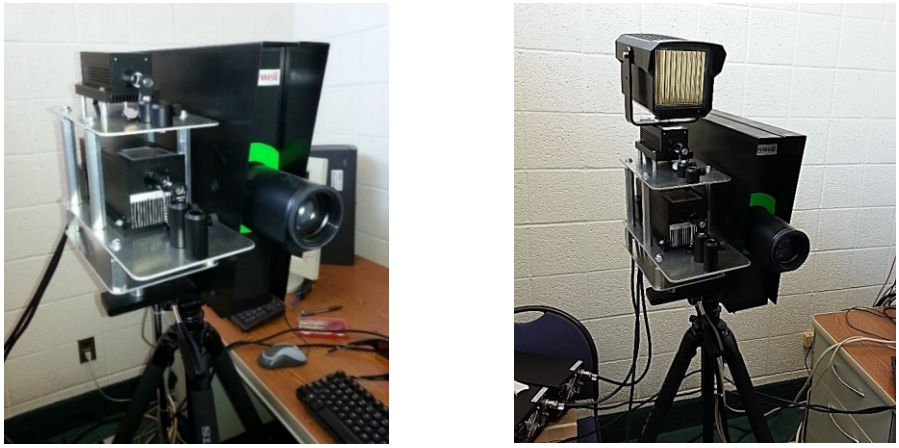

Figure 4.1. Dual SWIR illuminator in-lab set up (left) with original non-coherent IR illuminator configuration (right).

With fitting optics a rectangular illumination area of one meter squared at 8 feet was produced. Five OEM side vehicle front passenger/driver side window samples were purchased for four 2010 model vehicles and one 2013 model vehicle of different makes and styles, and structural and thickness designs (Table 4.1). The 2010 glass corresponded to a group of windows where spectral transmissivity properties into the first half of the lower band IR were quantified [12]. This corresponded to a side-fire configuration of illumination and the TBI to examine the passenger-side of the vehicle for occupants. Apparently, as in the vehicle windshield, newer vehicles apply solar glare blocking tint formulas to front passenger and driver side windows for safety and cabin comfort reasons.

Table 4.1. Front passenger side auto glass

OEM Glass Type	Make	Model	Year
FD21935GTY-Solar	Lexus	RX350	2010
FD22523GTN-Solar	Volvo	S40	2010
DD11163GTN-Solar	Chevrolet	Silverado	2010
DD09522GTN-Solar	Ford	Focus	2010
FD22542GTN-Solar	Volkswagen	Jetta	2013

4.2 INDOOR ILLUMINATOR RESULTS

The five auto glass types comparing the old illuminator and utilizing both illuminators are shown in Figure 4.2 through Figure 4.6, without any contrast enhancement of either band for each of the window types listed in Table 4.1. Within each four-image block in the figures, the upper left image is the TBI lower band IR spectral image (less than 1400nm), the upper right image is the upper band IR spectral image (greater than 1400nm), the bottom left image is the weighted subtraction of the two SWIR spectral images using multiplicative weights { K_{Lower} , K_{Upper} } in equation (3.2), and the bottom right image is the resulting binary image using a tolerance grey value, $0 \leq T \leq 1.0$. In all experiments the binary image is filtered using morphological closing (erosion followed by dilation) operation to improve segmentation and to filter out noise. With either active illumination test condition, penetration through the windshield was not achieved. Figure 4.7 illustrates the skin segmentation without vehicle glass obstructing the subject. Note that for the latter case, slightly larger weights were adjusted for the old illuminator in order to achieve similar detection characteristics for the test conditions that both illuminators. This might be explained by an 'additive' affect between the coherent prototype and non-coherent illumination devices.

Old Illuminator

K_{Lower} =0.8, K_{Upper} =1.6, T=0.20

Old Illuminator + Laser Illuminator

K_{Lower} =0.7, K_{Upper} =1.5, T=0.20

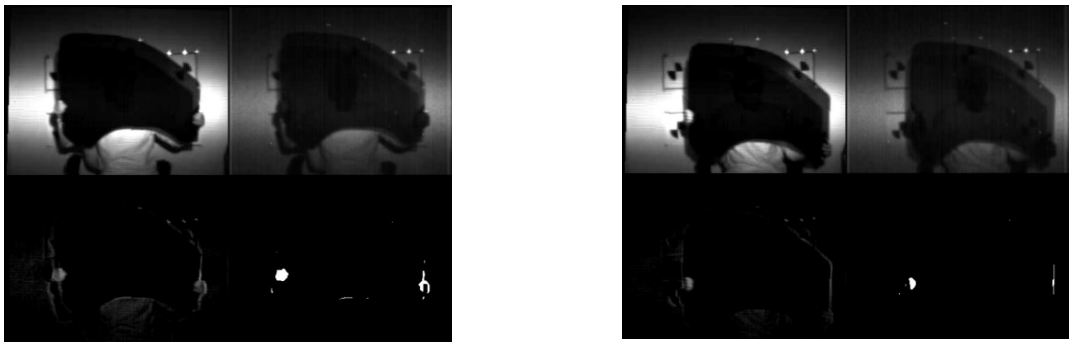

Figure 4.2. TBI human skin detection through Chev. Silverado. front passenger window.

Old Illuminator

K_{Lower} =0.8, K_{Upper} =1.6, T=0.20

Old Illuminator + Laser Illuminator

K_{Lower} =0.7, K_{Upper} =1.5, T=0.20

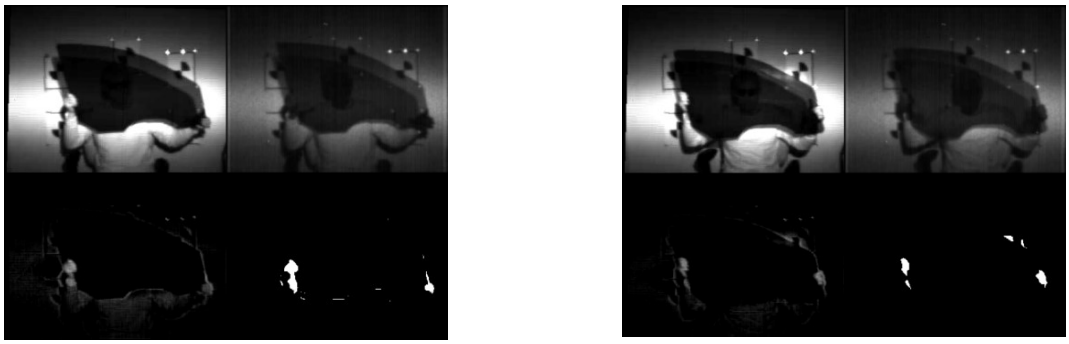

Figure 4.3. TBI human skin detection through Ford Focus front passenger window.

Old Illuminator

K_{Lower} =0.8, K_{Upper} =1.6, T=0.20

Old Illuminator + Laser Illuminator

K_{Lower} =0.7, K_{Upper} =1.5, T=0.20

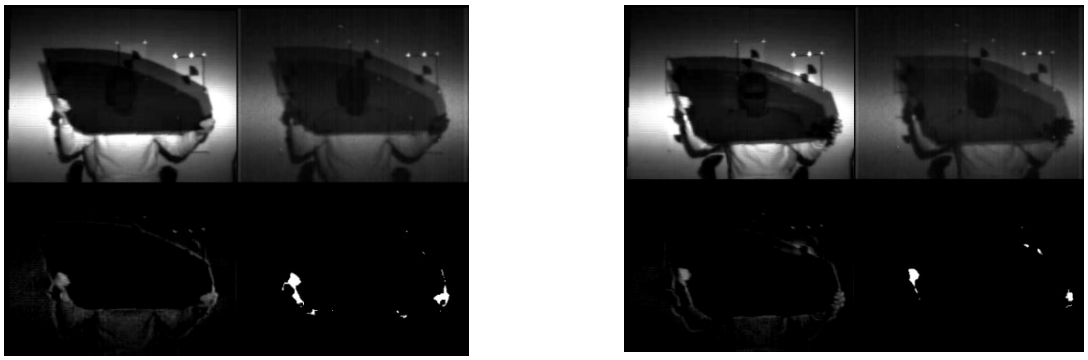

Figure 4.4. TBI human skin detection through VW Jetta front passenger window.

Old Illuminator

K_{Lower} =0.8, K_{Upper} =1.6, T=0.20

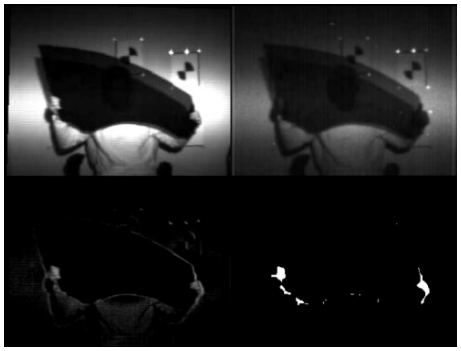

Old Illuminator + Laser Illuminator

K_{Lower} =0.7, K_{Upper} =1.5, T=0.20

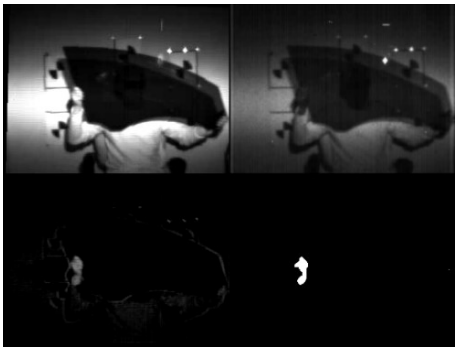

Figure 4.5. TBI human skin detection through Volvo S60 front passenger window.

Old Illuminator

K_{Lower} =0.8, K_{Upper} =1.6, T=0.20

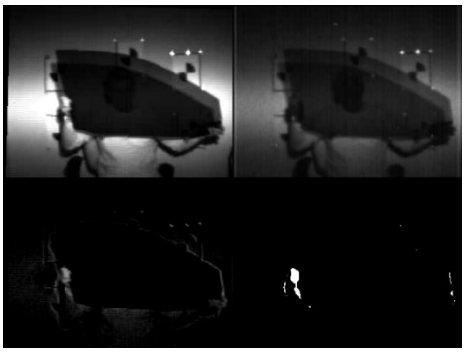

Old Illuminator + Laser Illuminator

K_{Lower} =0.7, K_{Upper} =1.5, T=0.20

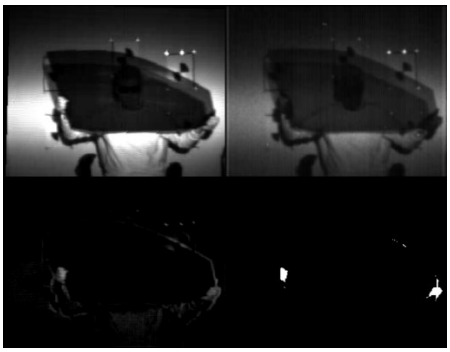

Figure 4.6. TBI human skin detection through Lexus RX350 front passenger window.

Old Illuminator

K_{Lower} =0.8, K_{Upper} =1.6, T=0.20

Old Illuminator + Laser Illuminator

K_{Lower} =0.7, K_{Upper} =1.5, T=0.20

Figure 4.7. TBI human skin detection without window glass obstruction.

The same video frames were then pre-processed using uniform histogram equalization for both the lower and upper SWIR bands to stretch the contrast over 256 gray levels (Figure 4.8 through Figure 4.12). The subject is clearly revealed both through the lower band and upper band images across both illuminator test conditions. Note that the multiplicative weights, K_{Lower} and K_{Upper}, were adjusted referencing the unobstructed skin detection and segmentation test condition (Figure 4.13). The facial skin in the difference images becomes evident primarily with the dual-laser tests, although even with these cases the difference proved too small to reliably segment from non-skin areas. Regardless of the illuminator, the improvement using this simple processing step is obvious.

Old Illuminator

K_{Lower} =1.1, K_{Upper} =1.4, T=0.20

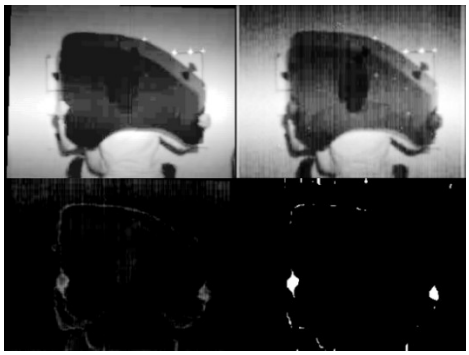

Old Illuminator + Laser Illuminator

K_{Lower} =1.1, K_{Upper} =1.4, T=0.20

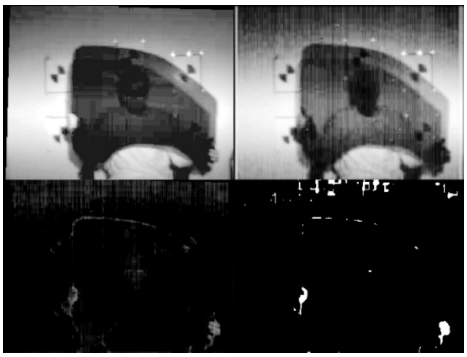

Figure 4.8. Uniform contrast histogram equalized TBI human skin detection through Chev. Silverado front passenger window.

Old Illuminator

K_{Lower} =1.1, K_{Upper} =1.4, T=0.20

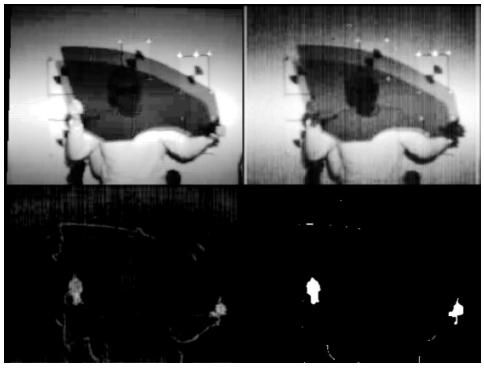

Old Illuminator + Laser Illuminator

K_{Lower} =1.1, K_{Upper} =1.4, T=0.20

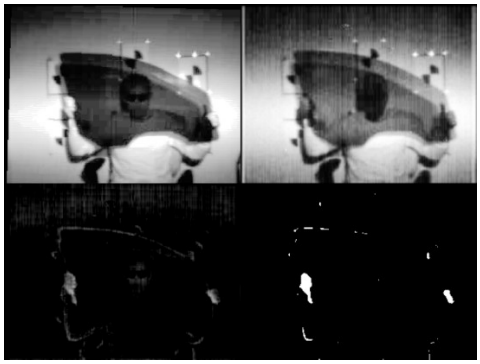

Figure 4.9. Uniform contrast histogram equalized TBI human skin detection through Ford Focus front passenger window.

Old Illuminator

K_{Lower} =1.1, K_{Upper} =1.4, T=0.20

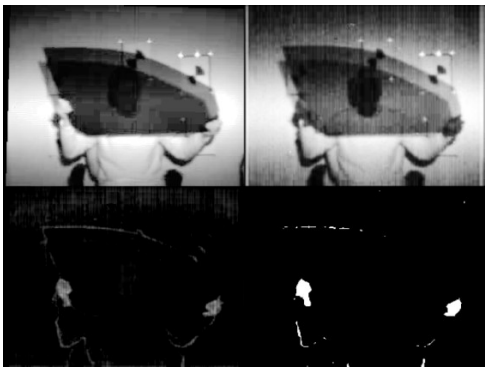

Old Illuminator + Laser Illuminator

K_{Lower} =1.1, K_{Upper} =1.4, T=0.20

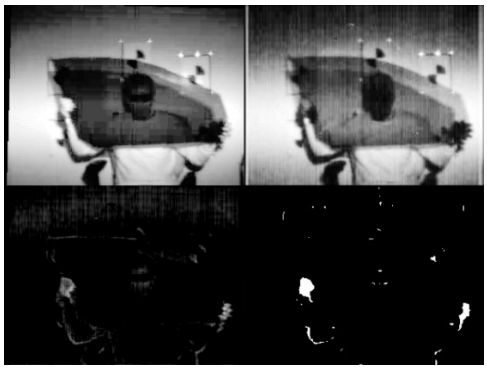

Figure 4.10. Uniform contrast histogram equalized TBI human skin detection through VW Jetta front passenger window

Old Illuminator

K_{Lower} =1.1, K_{Upper} =1.4, T=0.20

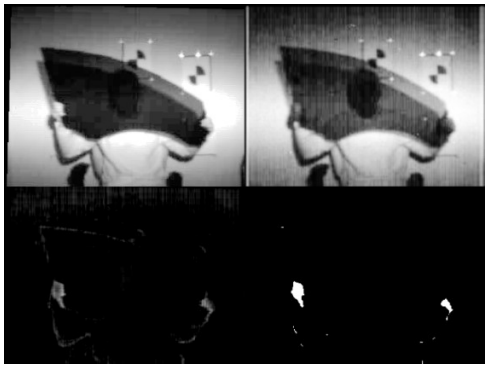

Old Illuminator + Laser Illuminator

K_{Lower} =1.1, K_{Upper} =1.4, T=0.20

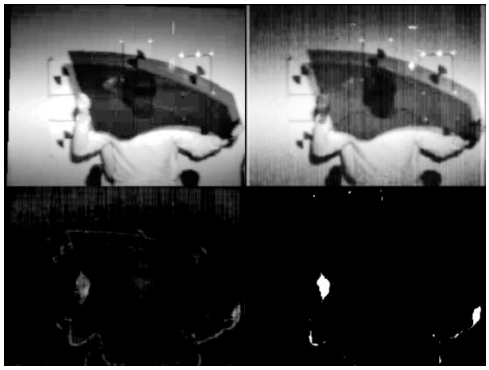

Figure 4.11. Uniform contrast histogram equalized TBI human skin detection through Volvo S60 front passenger window.

Old Illuminator

K_{Lower} =1.1, K_{Upper} =1.4, T=0.20

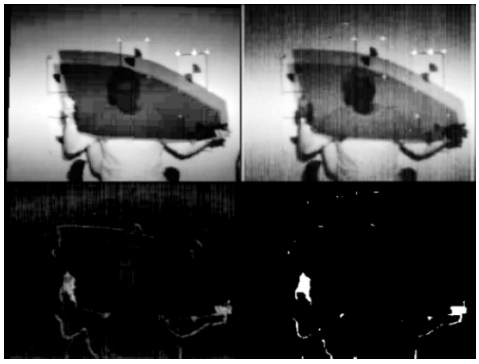

Old Illuminator + Laser Illuminator

K_{Lower} =1.1, K_{Upper} =1.4, T=0.20

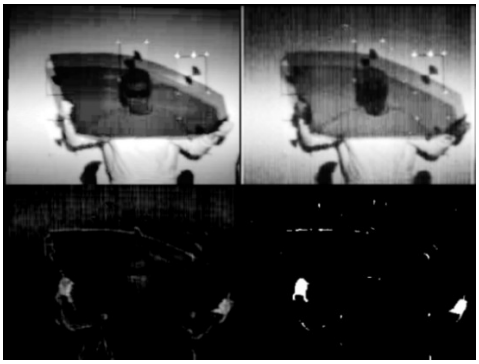

Figure 4.12. Uniform contrast histogram equalized TBI human skin detection through Lexus RX350 front passenger window.

Old Illuminator

K_{Lower} =1.1, K_{Upper} =1.4, T=0.20

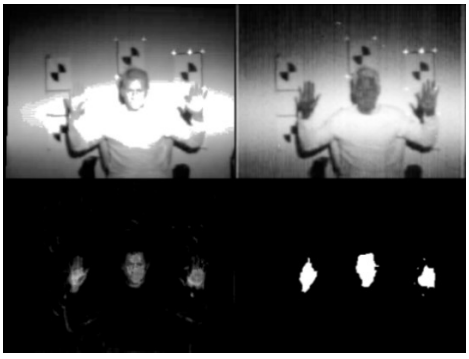

Old Illuminator + Laser Illuminator

K_{Lower} =1.1, K_{Upper} =1.4, T=0.20

Figure 4.13. Uniform contrast histogram equalized TBI human skin detection without a window obstruction.

The third test again utilized the same video sequence with a region of interest (ROI) defining an approximate boundary around the vehicle glass. It is assumed, under such a scenario, that the approximate ROI of either the passenger side window or windshield region can be discriminated as already documented in the literature [7], [11]. The identical histogram equalization contrast enhancement process was then carried out within the defined ROI (Figure 4.14 through Figure 4.18).

Old Illuminator

K_{Lower} =1.1, K_{Upper} =1.4, T=0.08

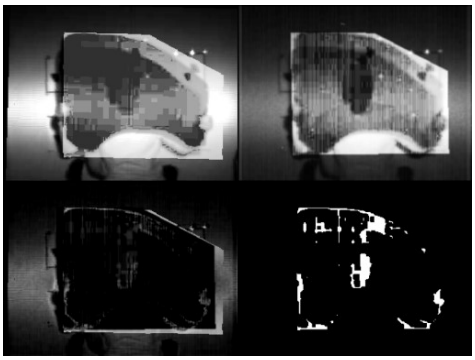

Old Illuminator + Laser Illuminator

K_{Lower} =1.1, K_{Upper} =1.4, T=0.20

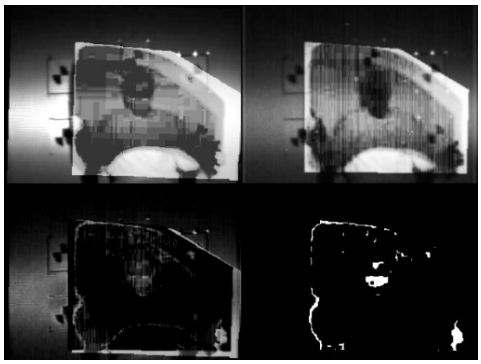

Figure 4.14. Region-based uniform histogram equalized TBI human skin detection through Chev. Silverado front passenger window

Old Illuminator

K_{Lower} =1.1, K_{Upper} =1.4, T=0.08

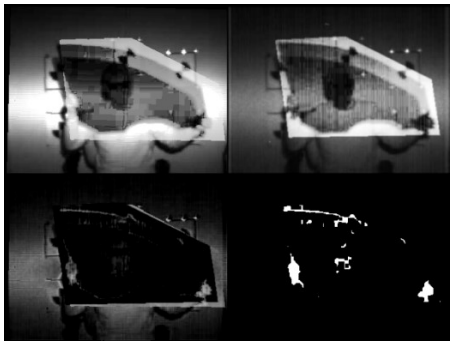

Old Illuminator + Laser Illuminator

K_{Lower} =1.1, K_{Upper} =1.4, T=0.20

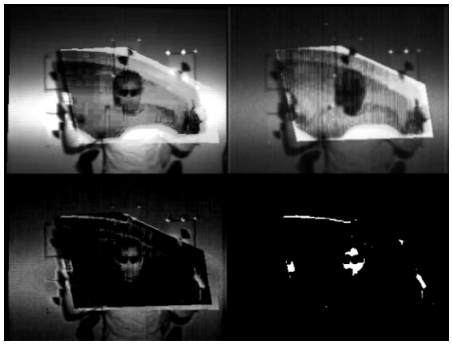

Figure 4.15. Region-based uniform histogram equalized TBI human skin detection through Ford Focus front passenger window.

Old Illuminator

K_{Lower} =1.1, K_{Upper} =1.4, T=0.08

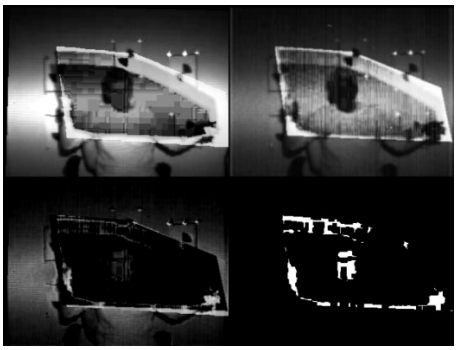

Old Illuminator + Laser Illuminator

K_{Lower} =1.1, K_{Upper} =1.4, T=0.20

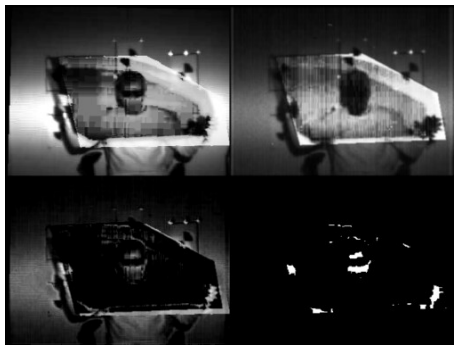

Figure 4.16. Region-based uniform histogram equalized TBI human skin detection through VW Jetta front passenger window.

Old Illuminator

K_{Lower} =1.1, K_{Upper} =1.4, T=0.08

Old Illuminator + Laser Illuminator

K_{Lower} =1.1, K_{Upper} =1.4, T=0.20

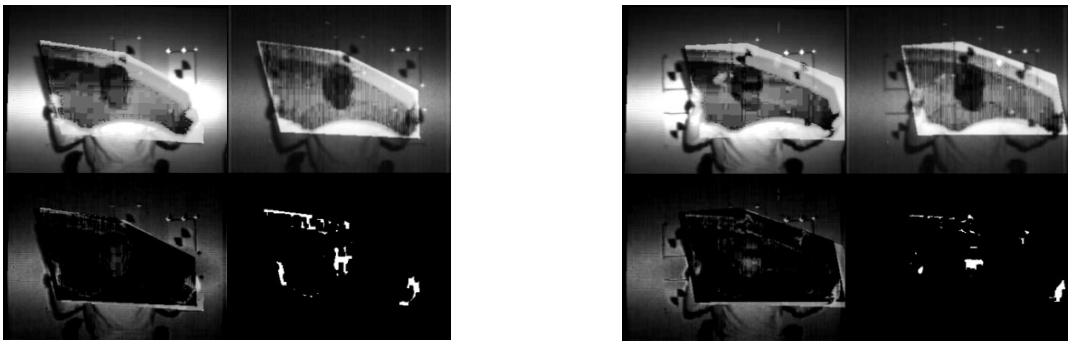

Figure 4.17. Region-based uniform histogram equalized TBI human skin detection through Volvo S60 front passenger window

Old Illuminator

K_{Lower} =1.1, K_{Upper} =1.4, T=0.08

Old Illuminator + Laser Illuminator

K_{Lower} =1.1, K_{Upper} =1.4, T=0.20

Figure 4.18. Region-based uniform histogram equalized TBI human skin detection through Lexus RX350 front passenger window.

Old Illuminator

K_{Lower} =1.1, K_{Upper} =1.4, T=0.08

Old Illuminator + Laser Illuminator

K_{Lower} =1.1, K_{Upper} =1.4, T=0.20

Figure 4.19. Region-based uniform histogram equalized TBI human skin detection without window obstructions.

Clearly, the improvement of skin detection was significant for both of the illuminator cases. Generally, no more than about half of the skin could be detected compared to detection without the glass obstructing the subject. There is a slight performance degradation with the single original TBI illuminator (more 'noise' of non-skin features), although generally the skin area detection relative to the unobstructed skin detection demonstrate similar outcomes (Table 4.2, T=0.0482, $p < 0.05$). What is less obvious- but of equal import, is that the binary threshold parameter to discriminate between the skin and non-skin surfaces was reduced by more than a factor of two from the dual illuminator threshold value (0.08 vs. 0.20). The final threshold value was adjusted such that the relative blob areas of a defined head region between the two illumination cases were nearly equivalent. Such a low threshold was very close to the noise (detectability) of the TBI imaging sensors; a lower threshold value resulted in far more non-skin 'noise' in the binary blob image (e.g., 'false negative' skin detection). Increasing the weights $\{K_{Lower}, K_{Upper}\}$ in equation (3.2), for either SWIR bands accentuated the image noise after uniform contrast equalization, and consequently led to a similar outcome.

Table 4.2. Relative blob size of subject face

Vehicle Glass	**% Face Blob Area** **Relative to non-glass face skin detection**	
	Both Illuminators	**Original Illuminator Only**
Chev Silverado 2010	45.45	55.88
Ford Focus 2010	46.62	17.54
VW Jetta Sedan 2013	44.08	47.23
Volvo S60 2010	28.86	30.87
Lexus RX350 2010	37.32	48.95
	40.47 ±7.42	**40.09 ±15.59**

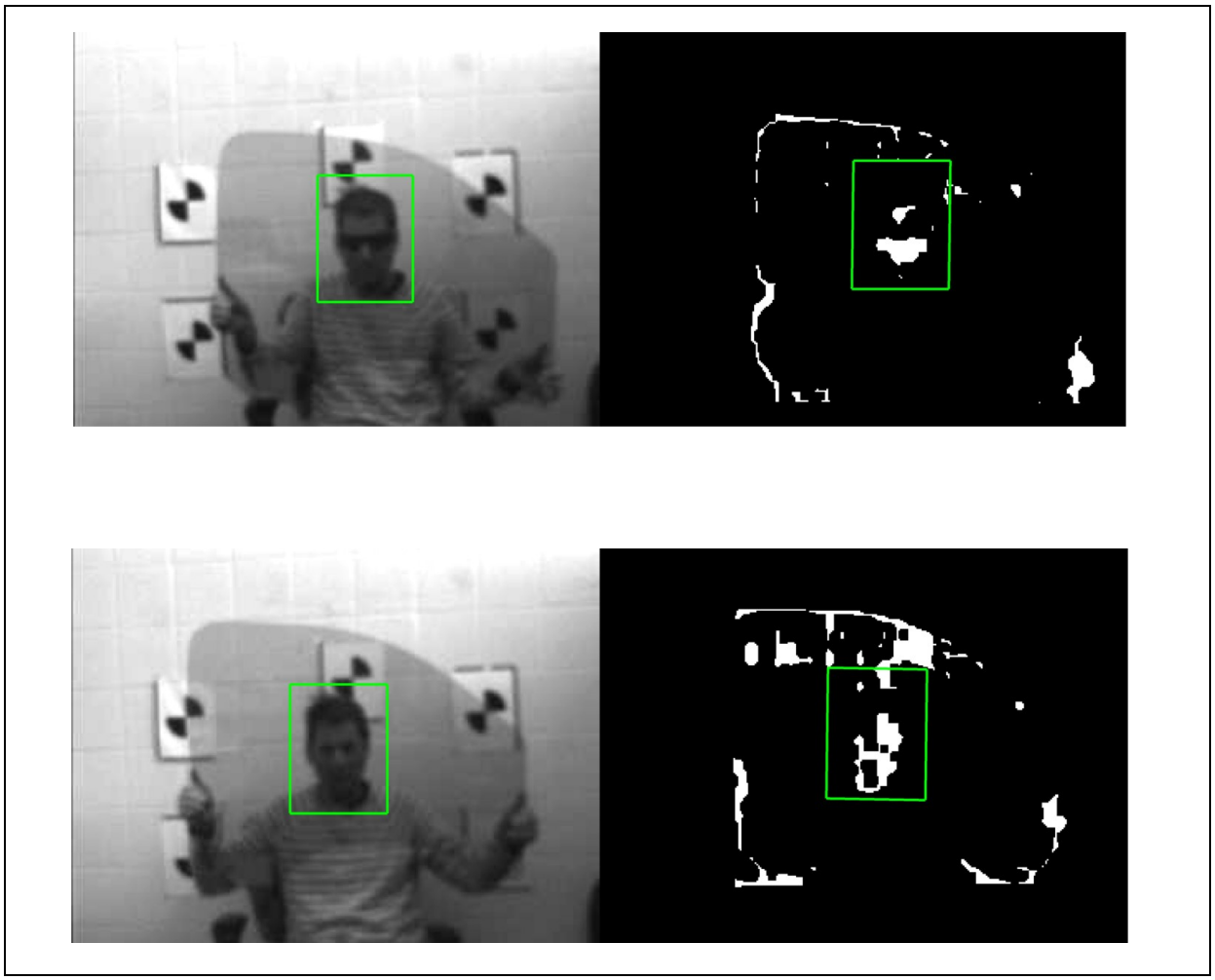

Figure 4.20. Example head ROI used for table 2 calculations, Chev. Silverado Passenger side glass. Top: both illuminators; bottom: Original TBI Illuminator only.

4.3 INDOOR ASSESSMENT CONCLUSIONS

The results of these experiments demonstrated that the TBI sensor was capable of penetrating through commonly manufactured vehicle glass to detect human subjects. These experiments indicated detection performance was affected by illumination power, even with relatively modest power increases within coherent bands residing within the lower and upper band spectral ranges of the TBI. Region-based contrast enhancement algorithms significantly improved detection capability with either tested illumination configuration. However, refining this approach for subsequent field deployments can introduce eye-safety hazards, which need to be addressed before such an arrangement could safely be deployed. For example, we could not energize the added laser illuminators outdoors due to such safety concerns. In short, penetrating the windshield is a far more complex, yet fundamental, problem that must be understood before deploying any such system for HOT/HOV lane enforcement.

CHAPTER 5: TBI FIELD EXPERIMENTS

Several controlled outdoor experiments were conducted to evaluate the effects of relative positioning of vehicles with respect to the sensor and illumination levels. To summarize, several repeated controlled experiments were done using three "typical" passenger vehicles from different manufacturers to understand and quantify their effects, across different environmental conditions. The indoor experiments suggested image processing enhancements were required to provide more robust in-vehicle human occupancy detection, which was then further refined and tested as part of these experiments.

In one set of experiments, all data were collected during overcast daytime conditions. The vehicles were also positioned away from potentially any direct sunlight. Therefore, the relative affect from the added IR energy in the SWIR band from the sun was minimized. It was evident from these experiments that significant reflective glare in the visible range limited the ability of the visible band from seeing occupants through the windshield. On the other hand, within the SWIR range, enough penetration occurred in the upper IR band (1400 nm < λ < 1700 nm) to identify human occupants. SWIR was associated with more consistent penetration than the lower SWIR band (900nm < λ < 1400 nm). Naturally, the question then arose how sunlight might affect detection capabilities under the same configuration scenarios. A second set of experiments where therefore conducted in direct sunlit conditions. The following summarizes these findings as well as algorithm refinements that can be used for skin detection.

5.1 EXPERIMENTAL DESCRIPTION

5.1.1 IR Illumination

Commercial off the shelf high power incandescent spot light designs were pursued that could be modified to output IR light. According to information from many of the manufacturers of such spot lights, which were engineered for theatrical and stage productions, many of the parabolic reflectors within the devices utilized dichroic material layers over the reflector to effectively cancel out the IR spectral band of the projected beam. Four 575 Watt AmericanDJ follow spots were acquired to provide the illumination source (ADJ FS-1000). Importantly, these illuminators use silver surface conic reflectors and thus the projected light in the infrared range required for the sensor was not attenuated. Infrared filter plates were machined to mount on the front of spot illuminators. Like other follow-spot lights, the beam cone angle can be varied and focused to different spot sizes. The plate material, which is abrasion resistant and low cost, has a ½ cut-off wavelength of at 708nm, with about 90 percent transmission throughout the SWIR spectral band of the sensor (950nm to 1700nm, Edmund Scientific, Optical Long Pass Filter #46-621). The filtered light output was still visible as a 'crimson' stop light glow at full power. Of course, the experiments could have been conducted without the filter plates, but it was important to utilize the filters in order to reduce visible lighting and glare affects from the illuminators particularly if they were to be pointed directly at oncoming vehicles. The illuminators were mounted on 8-foot

industrial tripods. If such lamp illuminators were deployed along the roadside, a weather proof vented enclosure to protect the units from the elements would be required.

5.1.2 Sensor Apparatus and Vehicle Positioning

The illuminators were then focused to provide an approximately 22 degree spot size—nearly the largest angle setting possible, which equated to a 6 foot (1.8m) diameter at a distance of 15.3 feet (4.7m) and an 11 foot (3.4m) diameter, at a distance 28 feet (8.5m). The smaller projected spot beam spanned the front windshields of the test vehicles, while the wider 11 foot diameter spot beam at the 28 foot distance spanned just under a standard twelve foot wide traffic lane. The cone angle was kept constant to understand the effect of reduced irradiant flux relative to the vehicle's surface glass, by moving the vehicle closer to the source. The group of illuminators were then closely arranged in a row together between eight to fifteen feet laterally from the TBI sensor. A vehicle was then positioned longitudinally either 15 feet, or 28 feet from the sensor, with a lateral offset of either twelve or six feet (Figure 5.1). Several repeated experiments were then conducted by varying eight shutter speeds of the TBI SWIR sensors from the fastest (250 μsec) to slowest speed (16 msec) (Table 5.1).

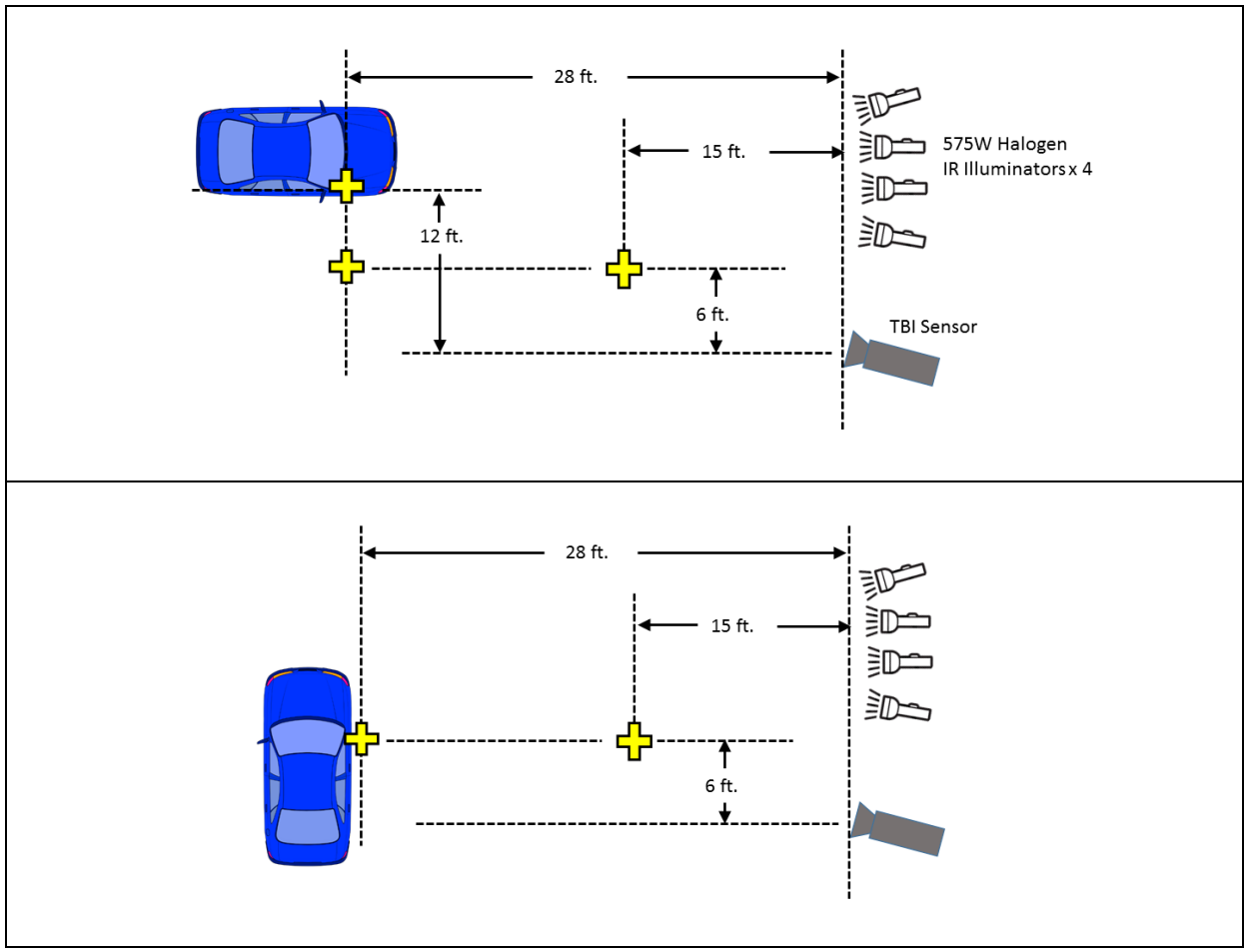

Figure 5.1. Outdoor experiment vehicle positions; TOP: oncoming head-on; BOTTOM: side-view.

Figure 5.2. Illuminator and TBI with side vehicle test.

Three test vehicles were used for all outdoor experiments: A black Volkswagen Jetta 2013 SE Sedan, a 2006 grey Mercury Mariner, and red 2016 Model Ford Fusion. We tested both "single occupancy" and "passenger occupancy" conditions across the several exposure settings that can be programmed to operate within the TBI sensor for experimental purposes. To understand any effect of the illuminators themselves, data were also collected with the illuminator off at the TBI default setting of sixteen milliseconds.

5.1.3 Outdoor Test Conditions

For the sake of brevity in the ensuing discussion, we define the three front facing conditions, with the two relative sensor longitudinal distances of twenty eight and fifteen feet, and two lateral distances of six and twelve feet as {*longitude distance*} × {*lateral distance*}.

For each of these position and vehicle combinations, the different programmable exposure times (global shutter periods) were configured equally for two SWIR band images. It was not possible to configure vary exposure times for the visible band camera. Table 5.1 summarizes an estimate of the irradiant energy density of SWIR illuminator across the programmable shutter exposure times of the SWIR TBI image sensors. The direct sunlight estimates in the same SWIR TBI lower and upper IR bands were derived from imperial data representing an average spectral irradiant flux of sunlight observed from the earth's surface. For the illuminators, the energy density levels are based on a blackbody emitter model. The energy density of the spectral irradiance at any given wavelength is estimated assuming uniform energy density across the projected overlapping focused spot sizes of the illuminators. The coverage area is estimated from the previously mentioned projected spot sizes. The calculations are based on 3200K temperature Tungsten Halogen bulbs totaling 2.3 KW x (~0.9 NIR filter transmittance) ≈ 2.07 KW of power.

Table 5.1. Estimated irradiant energy density for TBI SWIR bands

	Direct Sunlight		Tungsten Halogen Illuminator			
Integration Period (msec)	**LB Energy Density (mJ/cm^2)**	**UB Energy Density (mJ/cm^2)**	**15 ft. LB Energy Density (mJ/cm^2)**	**15 ft. UB Energy Density (mJ/cm^2)**	**28 ft. LB Energy Density (mJ/cm^2)**	**28 ft. UB Energy Density (mJ/cm^2)**
0.127	0.00202	0.00063	0.00292	0.00129	0.00084	0.00037
0.256	0.00403	0.00126	0.00584	0.00258	0.00168	0.00074
0.512	0.00806	0.00251	0.01169	0.00515	0.00335	0.00148
1.024	0.01613	0.00503	0.02337	0.01031	0.00671	0.00296
2.048	0.03226	0.01005	0.04674	0.02061	0.01341	0.00592
4.096	0.06452	0.02011	0.09349	0.04123	0.02683	0.01183
8.192	0.12903	0.04022	0.18697	0.08246	0.05366	0.02367
16.384	0.25807	0.08043	0.37395	0.16492	0.10732	0.04733
*16.67	0.26459	0.08246	0.3834	0.16909	0.11003	0.04853

*TBI default

5.1.4 Sensor Processing Algorithm

Instead of ROI-definition based histogram equalization, which can be sensitive to the region selected, a two-pass, contrast limited, adaptive histogram equalization was employed in both SWIR bands to localize the contrast enhancements within the vehicle windshield (or passenger side windows) [20]. The algorithm equalizes patches (a size of 5x5 was used) followed by a second pass normalization process

which clips max-intensity histogram peaks and then adds the remainder across other bins. Patch boundaries are interpolated between neighboring patches using bilinear interpolation to void edge artifact. Since the premise of the subtraction step is to create two separable distributions between low intensity and high intensity pixels, Otsu's algorithm was employed to calculate an optimal threshold in the difference image, instead of manually tuning the threshold. Thus, the parameter to vary is the ratio between the intensity multiplicative scale factors between the Lower to Upper SWIR bands to achieve skin segmentation. For the controlled lab experiments a gain ratio of the two multiplicative weights, $\frac{K_{Lower}}{K_{Upper}} < 1.0$, and we expected a similar finding for the outdoor experiments since the emitted Radiant power of the illuminators (and the sun) were relatively larger in the TBI lower band IR range than the upper band IR range. Morphological dissolve and dilation operators on the binary image were again used to create blobs, similar to the in-laboratory experiments. In the analysis a 4-sided polygon was used to isolate a region of interest (ROI) for windshields, and more generalized polygon shapes were used to define and isolate ROI for the front side windows (the ROIs were not needed however for the segmentation algorithm). The algorithm was implemented in OpenCV/C++ 3.0.

5.2 OUTDOOR EXPERIMENT RESULTS

For the non-illuminator experiments, only one case yielded positive skin detection (Table 5.2) primarily on the passenger side (lower band:upper band gain ratio=0.707). The lower and upper SWIR bands either achieved very low glass penetration that could not be differentiated from noise, or resulted in no penetration whatsoever. As expected, the positioning of the vehicles did not influence this result since the emitted radiant power cast upon the vehicles was independent of vehicle position. Figure 5.3 displays the result of the partially successful detection result, with the passenger side occupant face detected, while the driver occupant response was too weak for segmentation. The next several sections summarize results for each vehicle for both environmental conditions using the active illumination.

Table 5.2. Passive Illumination Results

Vehicle	Position	Orientation	Condition	Skin detection	Lower band penetration	Upper band penetration
Fusion	15x6	front	Sunny	fail	no,glare	no
Fusion	15x6	side	Sunny	fail	low	low
Fusion	15x6	side	Cloudy	fail	no	no
Fusion	28x12	front	Cloudy	fail	no,glare	no
Fusion	28x12	front	Sunny	fail	no,glare	no

Fusion	28x6	front	Sunny	fail	no,glare	no
Fusion	28x6	side	Sunny	fail	no,glare	no,glare
Fusion	28x6	side	Cloudy	fail	no	no
Jetta	15x6	front	Sunny	fail	no	no
Jetta	15x6	side	Cloudy	fail	no	no
Jetta	15x6	side	Sunny	fail	low	yes
Jetta	28x12	front	Sunny	fail	low	no
Jetta	28x12	front	cloudy	fail	no	no
Jetta	28x6	front	Sunny	fail	no,glare	no
Jetta	28x6	side	Sunny	fail	low	fair
Jetta	28x6	front	Cloudy	fail	no	no
Mariner	28x6	front	Sunny	Yes,partial	poor,glare	low
Mariner	28x6	side	Sunny	fail	low	low
Mariner	15x6	side	Cloudy	fail	no	no
Mariner	15x6	side	Sunny	fail	no	no
Mariner	15x6	front	Cloudy	fail	no	no
Mariner	15x6	side	Cloudy	fail	no	no
Mariner	28x12	front	Sunny	fail	no, glare	low
Mariner	28x12	front	Cloudy	fail	no	no

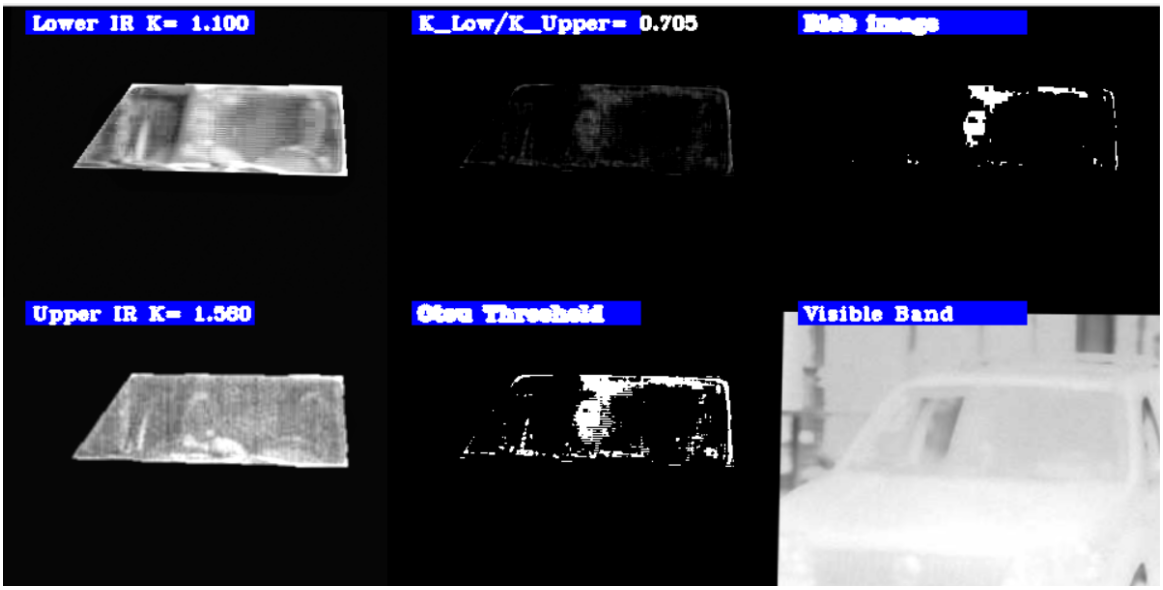

Figure 5.3. Mariner case, no illumination 28x12 sunny condition; images clockwise from upper left: Lower Band IR, Blob threshold, Upper Band IR, binary threshold, and visible band.

5.2.1 Volkswagen 2013 Jetta

5.2.1.1 Overcast Cloudy Condition

For the cloudy conditions, For the Jetta vehicle, segmentation could be achieved with the 4 millisecond minimum exposure, for 15x6 front facing vehicle position. An interesting observation was the upper band sensitivity to exposure and the light; windshield penetration in the lower band image was significantly less than upper band penetration. In particular, the skin reflectance in the lower band was insufficient for the differencing algorithm to be affective for the remaining exposures below 4 milliseconds. For the 28x6 windshield position, some penetration was achieved at the 16 millisecond exposures but object reflective glare in the lower band IR image precluded good segmentation using intensity differences, while the upper band was generally free of glare. Very little penetration past the windshield was observed for the next smaller exposure setting of 8 milliseconds; perhaps without the reflection anomalies at the lower band this experiment may have successful. Again, the lower band IR skin reflectivity was significantly diminished (as well as the glare phenomena). Note the windshield glare for these experiments in the visible band precluded the identification of the vehicle occupants. The same localized contrast enhancement algorithms were also applied to the visible band for these cases without any improvements in capability.

For the Jetta side window 15x6 experiment and largest 16 millisecond settings, a gain ratio of K_{lower}/K_{upper} = 1.085 was required to achieve modest penetration once again due to the fact that the skin reflectance was very low through the glass (even less than the windshield). With the window rolled down, the ratio could be reduced to 0.663 to achieve perfect segmentation, thus indicating the much lower relative

response of the lower IR band (Figure 5.5). The 8 millisecond exposure penetration could not be achieved due to similar reasons in the lower IR band as well as the shorter integration time. Interestingly, there was still a modest response in the upper IR band. No successful penetration was achieved for the 28x6 side window experiments. There was little reflective glare phenomena in any of the bands during the side window tests.

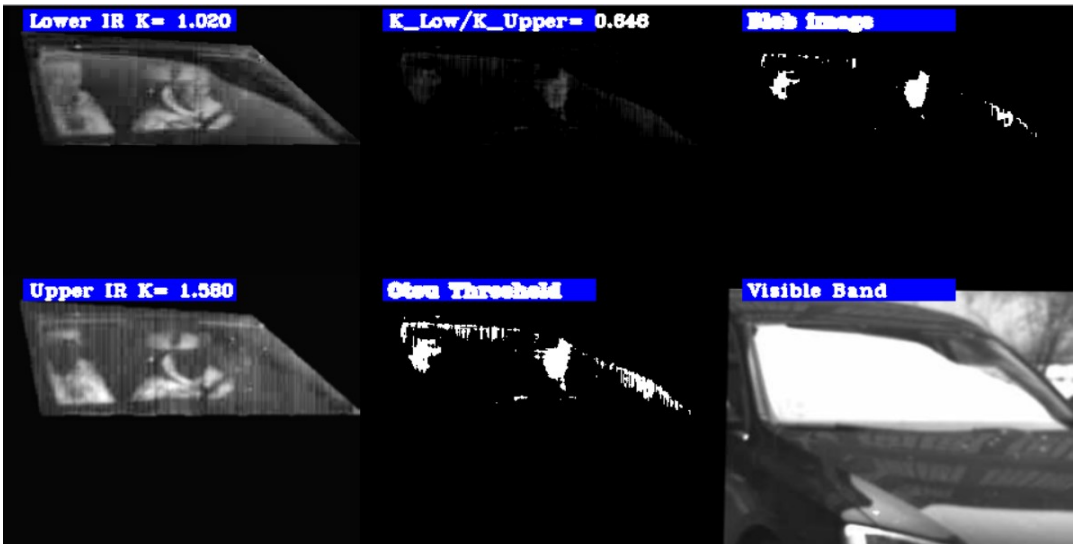

Figure 5.4. Volkswagen 2013 Jetta SE, 15X6 cloudy condition; images clockwise from upper left: Lower Band IR, Blob threshold, Upper Band IR, binary threshold, visible band.

Figure 5.5. Volkswagen 2013 Jetta SE, 15X6 side window, cloudy condition; TOP: window open, BOTTOM: window closed.

5.2.1.2 Sunny Condition

For Sunny conditions, initially the lens Iris setting was kept identical to the cloudy condition experiments. Thus, we would expect that shorter integration times could be achieved, as well as test the capability of the sensor with very high light energy input. For the 16 millisecond exposure settings during front windshield cases, too much glare in the Lower band IR interfered with the segmentation algorithm for skin detection of the occupant faces.

However, side 15x6 window case at the 16 millisecond exposure settings yielded clearer penetration than the cloudy case, with a gain ratio of 0.7 (the open window gain ratio was similar to the cloudy case, equal to 0.662). Note that the sunlight was relatively direct upon the passenger subject and very little

glare was apparent in the lower IR band image (Figure 5.6). Some penetration was achieved also at the 8 millisecond exposure setting albeit the lower band IR contrast of skin reflectance was noticeably less: the lower band to upper band gain ratio was increased to 0.917. Some side window glare in the visible spectrum image was evident for these cases. For the 4 millisecond exposure setting, any penetration and segmentation that could be achieved was confounded by sensor noise (the ratio was 1.80). None of the other exposure settings were capable of penetration. Furthermore, no segmentation could be achieved for any of the sunny 28x6 side window cases.

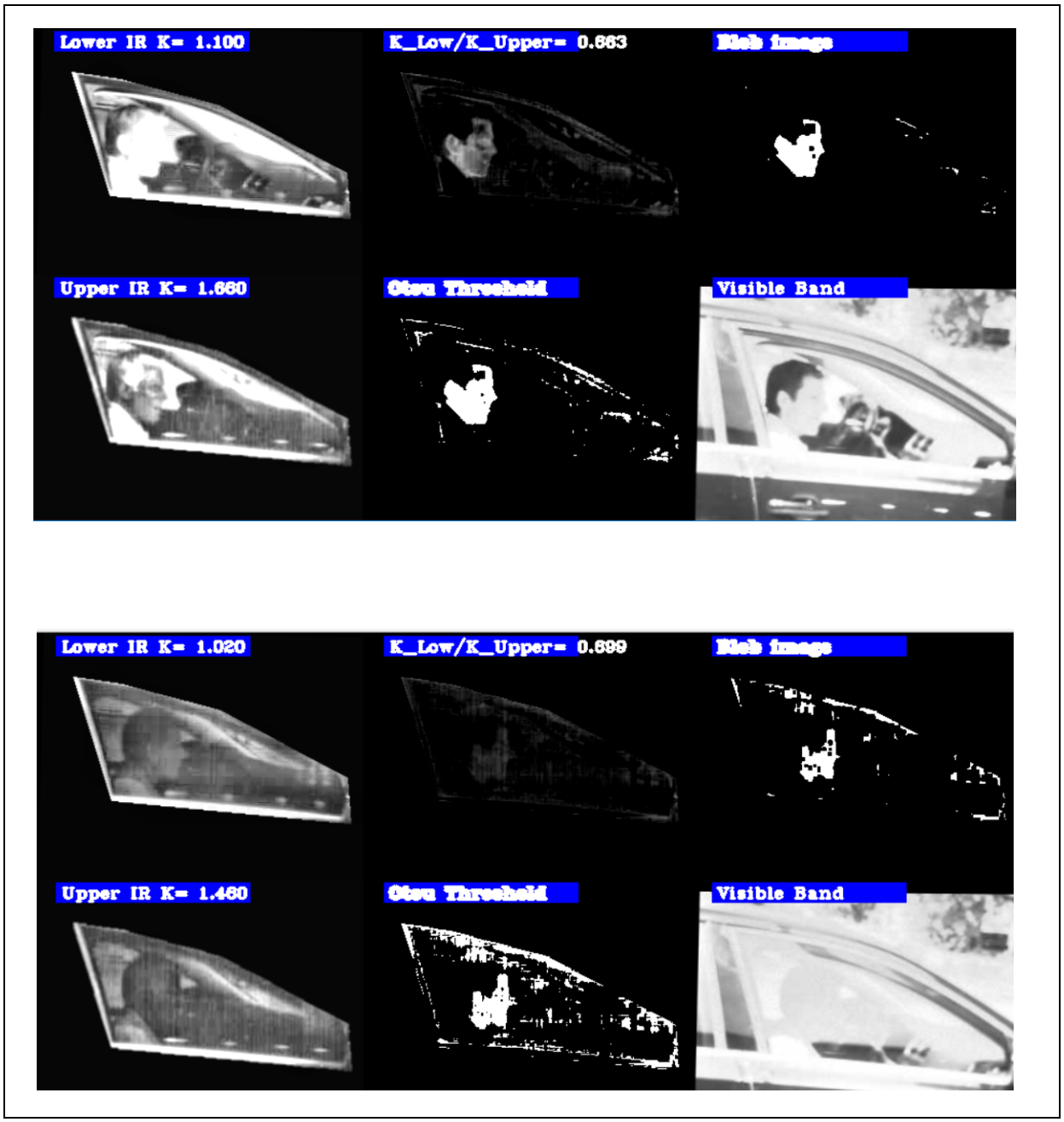

Figure 5.6. Volkswagen 2013 Jetta SE, 15x6 sunny condition; TOP: window rolled down.

5.2.2 Mercury 2007 Mariner

5.2.2.1 Overcast Cloudy Condition

For the 16 millisecond exposure setting 15x6 front window case, skin detection could be achieved (ratio=0.540). However, there was some glair affects in the lower band IR which created artifacts in the difference image that could not be removed by the differencing and segmentation algorithm alone. As in other experiments, the outcome is consistent between the sensor default exposure setting and the largest setting which are both near 16 milliseconds (ratio=0.455 vs. a ratio=0.540 for the 16 millisecond setting). For the 8 millisecond exposure time experiment the lower SWIR band exhibited low reflectivity of the skin, which was less than the reflected glare of the windshield and thus segmentation and detection was very limited. A ratio of 0.755 provided minimal skin detection at this integration period. None of the other remaining smaller exposure time periods proved to be successful.

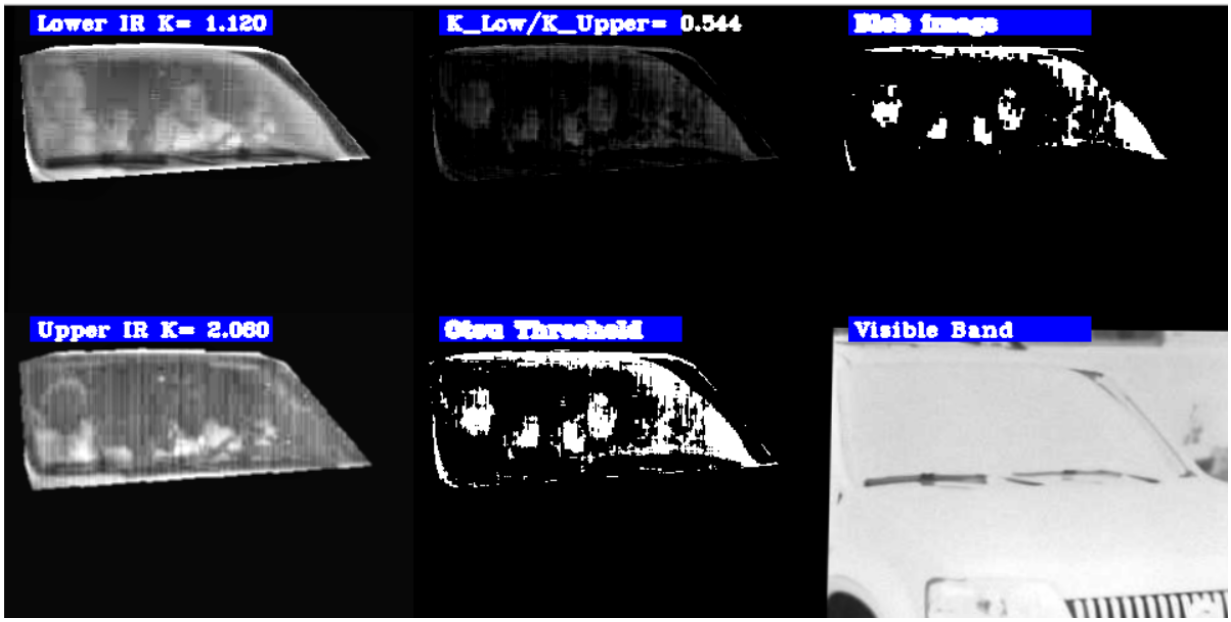

Figure 5.7. Mercury Mariner 2006, 15x6 cloudy condition; images clockwise from upper left: Lower band IR, Blob threshold, Upper band IR, binary threshold, visible band.

None of the 28x6 or 28x12 front facing positions were successful. Again, the intensity levels of reflective glare were equal to, or greater than, the skin reflectivity of the passenger and driver, which prevented reliable segmentation.

For side window tests on the cloudy condition, 15x6, (ratio=0.583), segmentation was achieved for the 16 millisecond exposure (ratio=0.651) cases, the glare was especially pronounced in the visible range, and similar to earlier windshield cases with the Jetta vehicle, it was difficult to make out the subject.

There was also observable reflections in the SWIR range as well (the lower band IR image was most prevalent) but the reflective intensity of the skin was high enough to mitigate much of this affect.

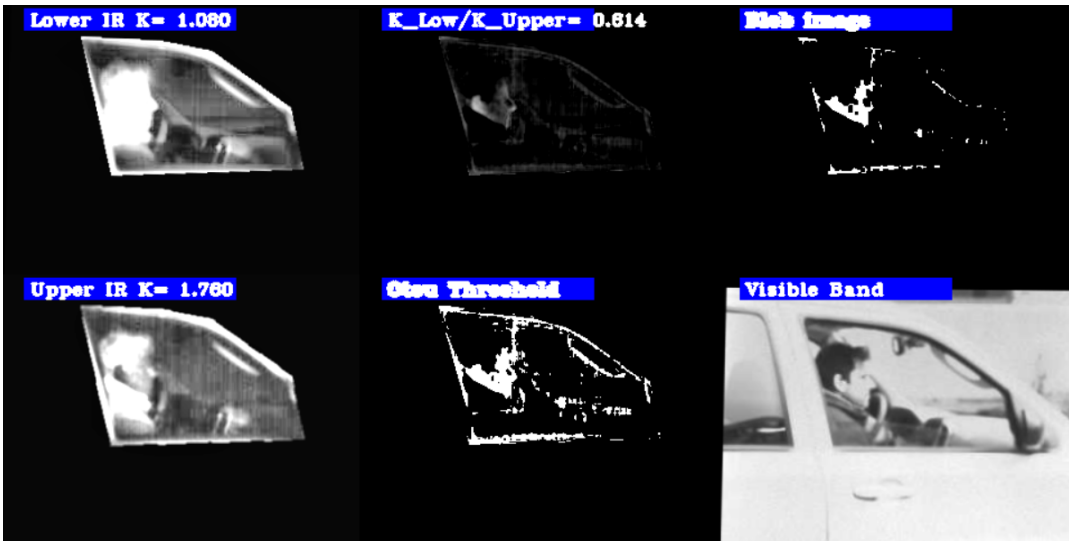

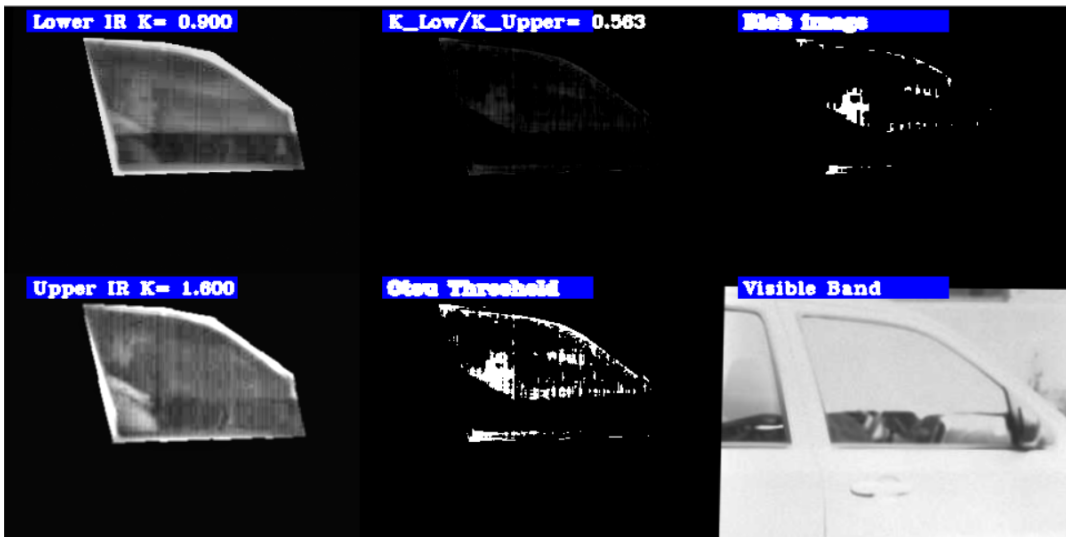

Figure 5.8. Mercury Mariner 2006, 15X6 side window cloudy condition; TOP: window open; BOTTOM: window closed.

For the 8 millisecond setting, the skin reflectivity intensities were too close in intensity to be segmented from the window glare and blooming intensities to achieve subject skin segmentation. No segmentation could be achieved for the passenger side 28x6 vehicle position experiments.

5.2.2.2 Sunny Condition

Although the subjects could be identified similar to the cloudy experiments for the sunny conditions, the sun glare off of the windshield produced especially high return intensities for all the exposure conditions, preventing any consistent segmentation of the occupant's skin. For the 28x6 position experiments, the default (ratio=0.811) and 16 millisecond exposure cases, the glare was also prevalent but some segmentation of the passenger could be achieved. Segmentation could not be achieved in any of the other 28 foot front or side vehicle orientations, again due to the level glare reflections from the vehicle windows.

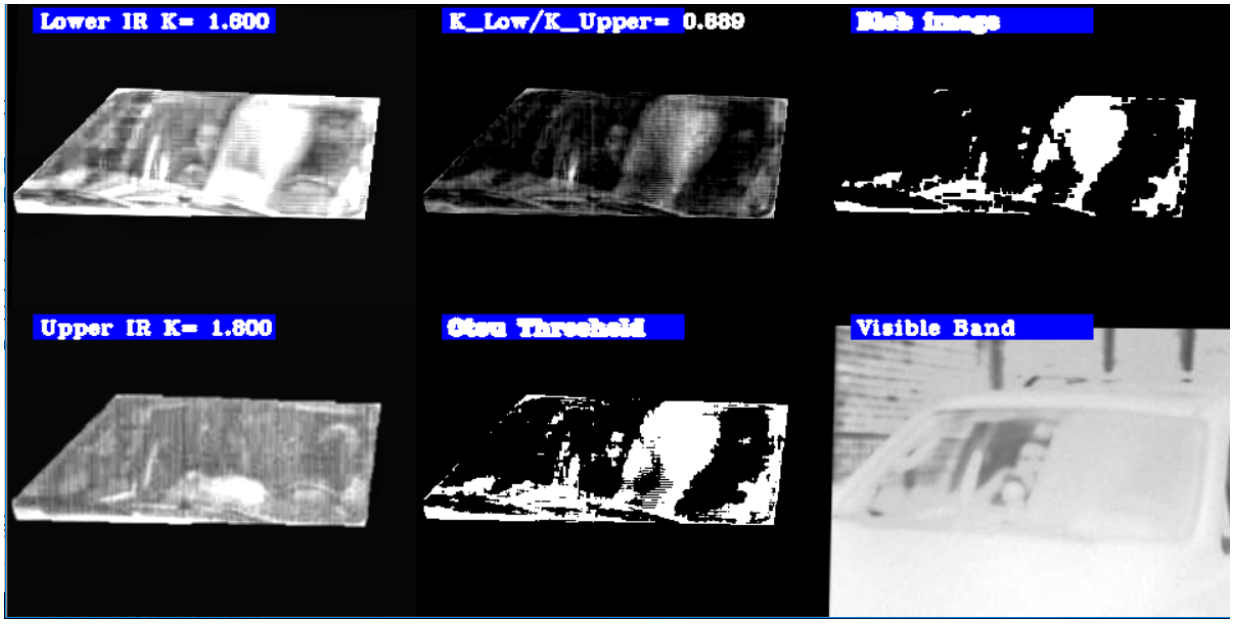

Figure 5.9. Mercury Mariner 2006, 15X6 sunny condition; images clockwise from upper left: Lower Band IR, Blob threshold, Upper Band IR, binary threshold, visible band. Subject visible but glare and blooming exceeded response of skin for subjects.

For the side window 15x6 positions during the sunny conditions, no segmentation was achieved, despite adjustments to iris as well as the integration times. No explanation can be offered why the sunlit cases during these experimental conditions resulted in very little penetration of either the TBI upper or lower SWIR bands, compared to the cloudy day cases.

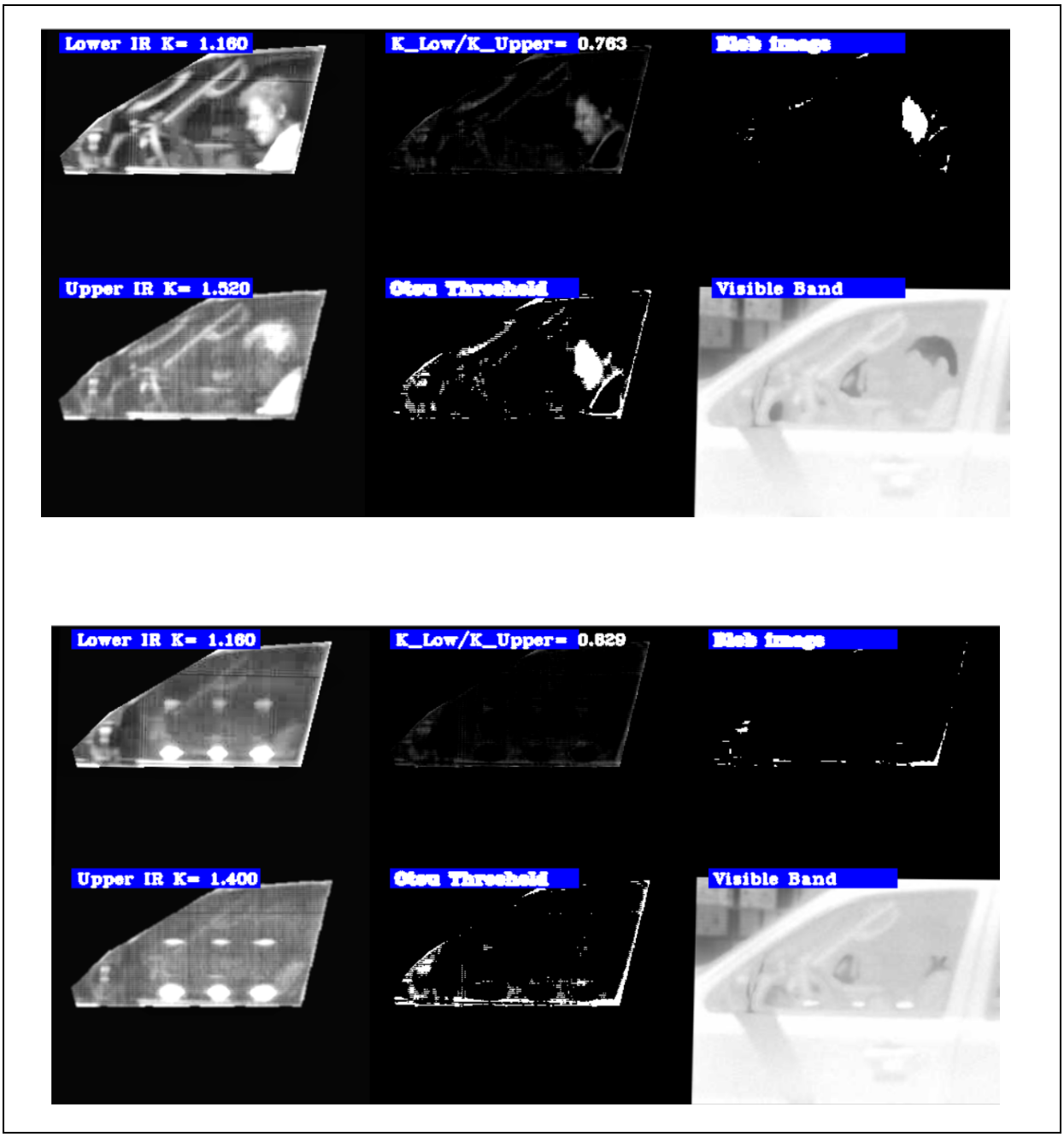

Figure 5.10. Mercury Mariner 2006, 15X6 side window sunny condition; TOP: window open; BOTTOM: window closed.

5.2.3 Ford 2016 Fusion

5.2.3.1 Overcast Cloudy Condition

Although penetration could be achieved with skin segmentation, for the Cloudy condition, (ratio=0.368), 15x6 front position sixteen millisecond exposure, there was significant object reflections (the side of a

building) off of the windshield surface which confounded the segmentation. In Figure 5.11, the reflection 'slices' half the faces of the occupants within the vehicle. The visible band was not correctly captured during these sets of experiments due to a hardware malfunction that occurred during the experiments. The 8 millisecond exposure time experiment was similar, (ratio=0.479) albeit the lower band IR reflections were weaker than the 16 millisecond exposure time experiments; segmentation was consequently reduced for this case. No segmentation and detection for all the remaining lower exposure time periods could be achieved.

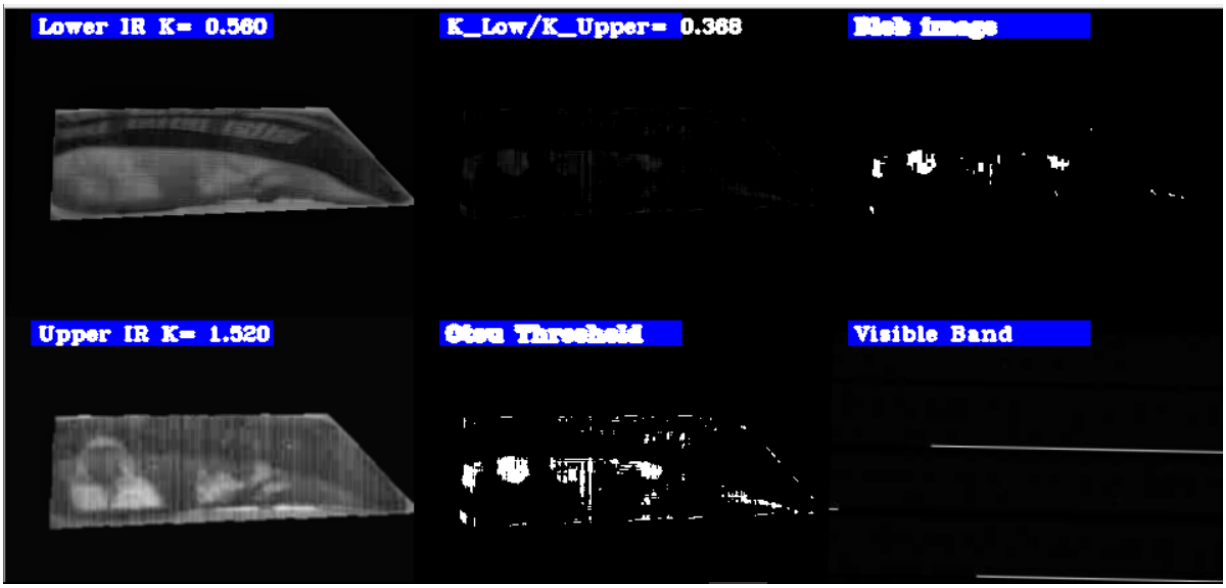

Figure 5.11. Ford Fusion 2016, 15X6, cloudy day; images clockwise from upper left: Lower Band IR, Blob threshold, Upper Band IR, binary threshold, (visible band not available).

For the side window cases, the default (ratio=0.73) condition at the 15x6 position experiment achieved partial segmentation; the penetration was too low, and near the noise margin even for the highest exposure times. The same experiment was repeated with a second subject which actually resulted in slightly better segmentation and skin detection with less reflection and noise artifact (ratio=0.71). The gain ratios did not change much for the unobstructed and closed window views of the subject's face. Side window glare was also prevalent (the visible band was recorded incorrectly due to cable and connection malfunctions that occurred during the experiments). The 8 millisecond exposure time was again too noisy in both bands to achieve reliable skin segmentation.

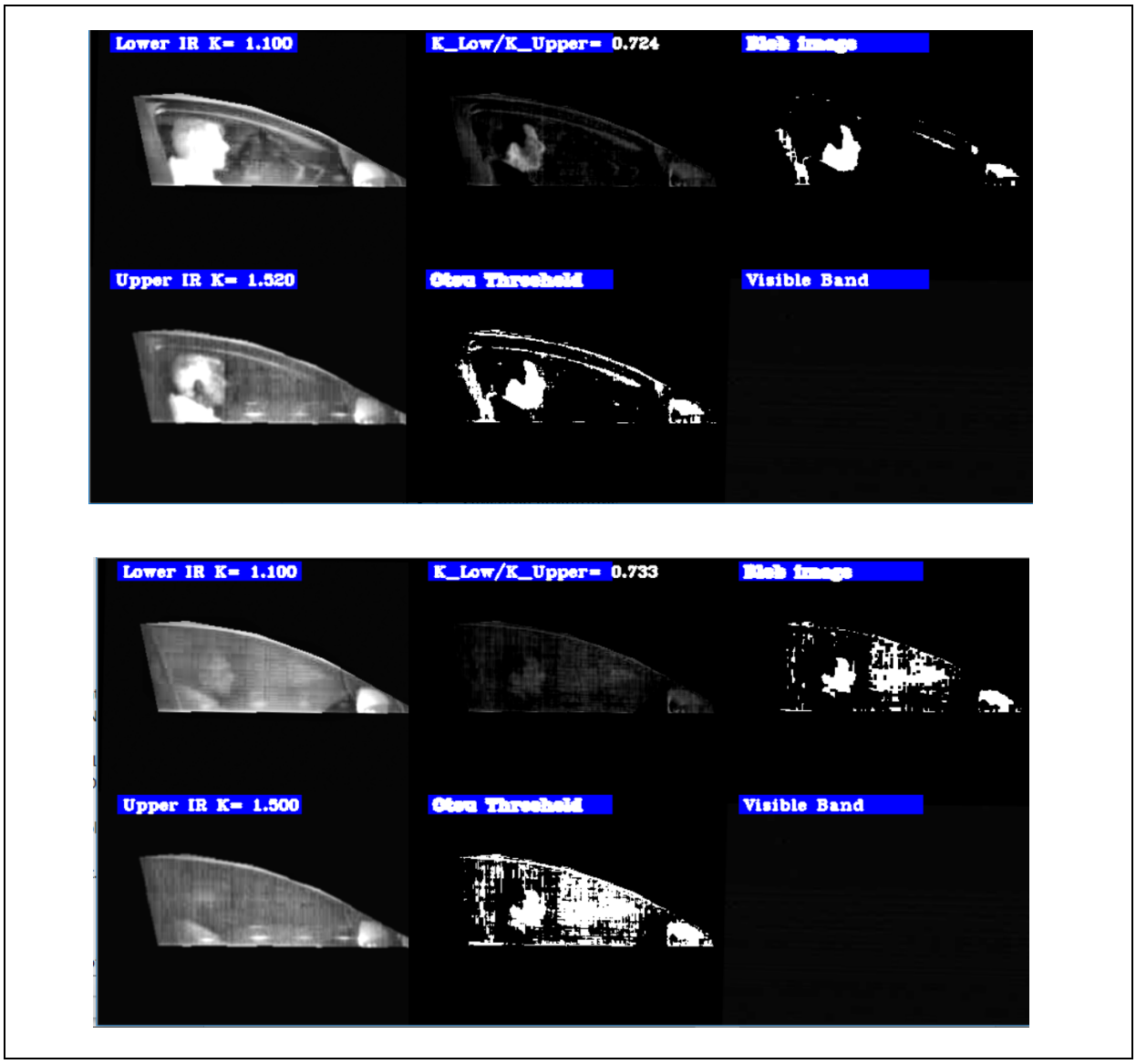

Figure 5.12. Ford 2016 Fusion, 15x6 side window sunny condition; TOP: window open; BOTTOM: window closed.

5.2.3.2 Sunny Condition

For this vehicle, detection could not be achieved for the sunny condition experiments. Although some penetration at both SWIR bands can be observed for the front windshield experiments, the reflections and glare were very pronounced and precluded any segmentation, since the intensities for these reflections either masked the subject or could not be discriminated from human passenger skin (Figure 5.13). Interestingly, side window cases actually yielded poorer results than the cloudy sky conditions.

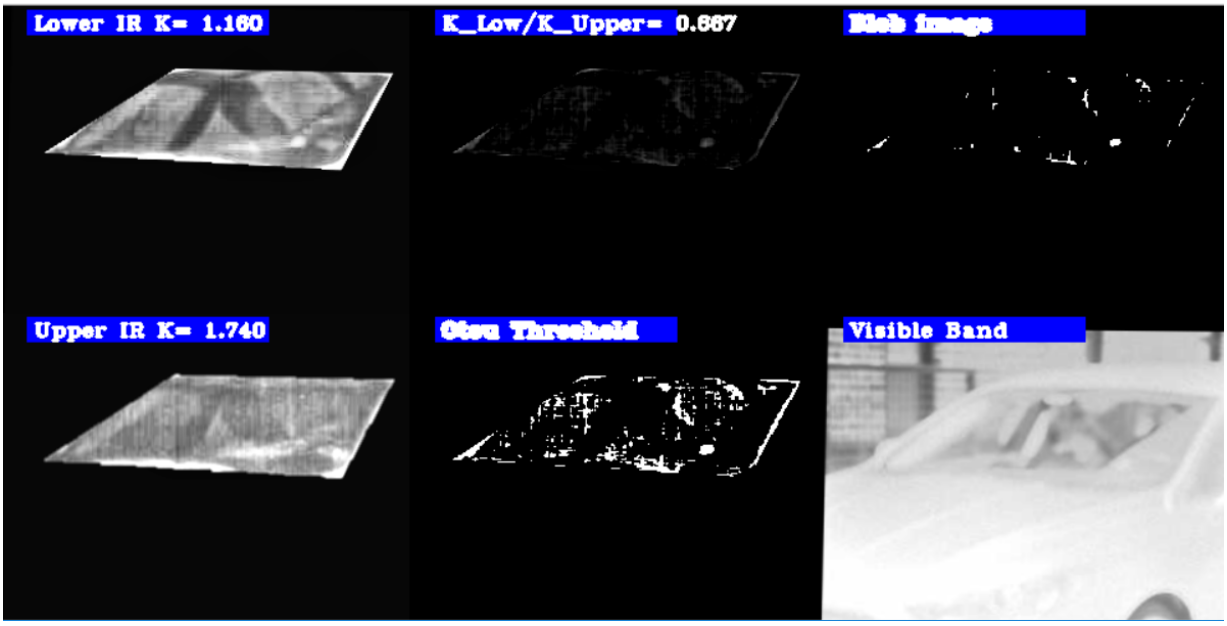

Figure 5.13. Ford 2016 Fusion, 15x6 sunny condition. Images clockwise from upper left: Lower band IR, Blob threshold, Upper band IR, binary threshold.

What is interesting is that there were significant reflections in the SWIR range for the Ford Fusion vehicle – particularly within the 950-1400nm SWIR lower band in both, the cloudy and the sunny conditions. For many experiment cases, the illumination power was insufficient to overcome this phenomena. As mentioned previously, it was nearly impossible to observe the occupant(s) for any experiments with the visible band image during cloud cover conditions (a cable and connection malfunction prevented recording of the visible band that would have illustrated this). As a final note, with the visible band images, the histogram equalization technique was also tested with the visible band images, in part to overcome the glare obstructions. Unlike the SWIR band, the technique was not able to reveal the occupants in any of the experiments.

5.3 CONCLUSIONS

Several repeated outdoor experiments for both cloudy and sunshine conditions with the TBI were performed using three “typical” passenger vehicles from different manufacturers to understand and quantify performance requirements for TBI implementation. The cloud cover conditions were not aided by any direct sun light, producing low ambient lighting conditions from an overcast sky, while during the sunny conditions, the vehicle windows faced into the sunlight. We had originally reasoned that increasing the light energy exposure would improve detection performance, for example during sunny vs. cloudy conditions. However, glare and other artifacts confounded detection utilizing pixel intensity alone. The experiments also suggest that the variability in transmissivity characteristics in vehicle glass had a significant effect on detection capability, although this was not quantified. Nevertheless, detection of human occupants through vehicle glass was certainly attainable for some conditions—such as those

away from directed sunlight or reflective glare. Furthermore, it is evident that the SWIR upper band imaging (1400 nm < λ < 1700 nm) was associated with more consistent penetration than the lower SWIR band image (950nm < λ < 1400 nm), even though spectral models indicate that the spectral energy in the SWIR lower band is greater than the upper SWIR band.

Interestingly, for the sunny day experiments, the added energy from direct sunlight showed no significant improvement and in fact, under many conditions, the glare and reflections could not be segmented from the human passenger subjects. Reflective glare observed within the lower SWIR band could not be removed using the pixel intensity thresholding approach, especially since the intensity of skin reflections through the vehicle glass was significantly attenuated compared to the direct exposure that was blocked by the vehicle glass.

The experiments suggests a minimum energy level requirement for both of TBI SWIR bands. Given the desired energy exposure times, equivalent irradiant flux levels can be estimated. In fact, the exposure times must be very short to accommodate image capture of high speed vehicles. For example, the estimate from [7,12] suggests an exposure time generally no more than 0.5 milliseconds to reduce pixel blur to a single pixel, or less for vehicles traveling at freeway speeds (65 miles per hour). Accordingly, an extrapolated total equivalent minimum illumination energy of over 9.4 Joules for the lower SWIR band, and 4.1 Joules in the upper SWIR band may be necessary for TBI operation (Table 5.3). This equates to a continuous illumination of power of at least ~8 KW in the upper SWIR band and ~19 KW in the lower SWIR band ≈ 27 KW at the aforementioned exposure time to perform human occupancy detection.

Table 5.3. Estimated SWIR illuminator energy output

Integration time (msec)	Lower Band Energy (mJ)	Upper band Energy (mJ)	Lower Band Energy Density (mJ/ cm^2)	Upper Band Energy Density (mJ/cm^2)
0.127	73.789	32.542	0.003	0.001
0.254	147.578	65.085	0.006	0.003
0.508	295.156	130.170	0.012	0.005
1.016	590.312	260.340	0.023	0.010
2.032	1180.625	520.679	0.047	0.021
4.064	2361.249	1041.359	0.093	0.041
8.128	4722.498	2082.718	0.187	0.082
16.256	9444.997	4165.435	0.374	0.165
16.667	9683.794	4270.750	0.383	0.169

More generally, the results of the experiments may be somewhat pessimistic since there have been significant improvements in detection capabilities of the SWIR sensors. Specifically, the normalized Detectability of recent SWIR sensors have improved by almost two orders of magnitude from those integrated within the TBI, according to published specifications (320HX-1.7RT, $D = 1.0 \times 10^{14}$ *cm·√Hz/*W vs. 3×10^{12} *cm·√Hz/*W for TBI SWIR sensors, Sensors Unlimited, Inc). The Detectability is an indication of the sensor sensitivity. Specifically, the normalized Detectability refers to the ratio of the responsivity of the SWIR sensor to the noise produced within the SWIR sensor detection technology [21]. This may significantly improve the capability to better resolve reflective intensity signals of exposed skin from signal 'noise'.

CHAPTER 6: EYE SAFETY RISK

Since the data indicated the importance of sufficient IR illumination in the upper and lower SWIR bands of the TBI sensor, an important aspect of deploying such a sensor is to assess eye safety hazard risks associated with directing active Infrared range illumination toward the oncoming motorists who would be passing through the sensor observation field. This study utilized continuously activated illumination. Laser illumination technologies may provide a solution which are superior to the aforementioned tested illumination methods as long as their use produces minimal eye safety hazards. For example, pulsed lasers conceptually operate similar to non-lasing flash lamp illuminators used in many early renditions of automated license plate number readers (ANPR) and red-light enforcement technologies (for example, Xenon flash lamps). A small or modest amount of energy is discharged in a very small time period, resulting in extremely high radiant power production. Depending on the laser cavity medium and pumping technology, a rapid succession (typically in several KHz range) of very short duration pulses (on the order of nanoseconds) can be achieved. The procedures evaluating this risk is summarized below.

6.1 MAXIMUM PERMISSIBLE EXPOSURE

Determining eye exposure risk is based on determining a Maximum Permissible Exposure that if exceeded increases the risk of injury to an 'unacceptable level'. The ANSI Z136.1 2007 standard defines the MPE as "the level of laser radiation to which an unprotected person may be exposed without adverse biological changes in the eye or skin. [22]" Such standardized dosage levels were determined by the US Center for Devices and Radiological Health (CDRH). The standards were developed particularly for coherent lasing sources. All such devices that output light power exceeding 5 mW must be registered and tested to indicate a standardized class associated with risk (Table 6.1). For example, the continuous wave lasers used for the indoor laboratory experiments discussed in Chapter CHAPTER 4: are class 4 devices.

What is missing from this table is influence of exposure time, frequency wavelength, and the temporal exposure characteristics (continuous vs. pulsed illumination), and actual irradiance level on the exposed surface (retinas). For example, a coherent IR source with a wavelength exceeding 1500nm is "Retina Safe" because the tissues in the eye before the retina will absorb almost all the IR light (However there is still a risk of damage to the cornea). Furthermore, beam power density (irradiance) exposed onto the eye affects the exposure time risk. This results in formulating a limiting aperture that is the calculated surface area based on the approximate diameter (~7 mm) of maximum retinal aperture of the human eye. Thus optical assemblies placed in front of the exit beam which spread out the energy to a lower density will therefore further reduce eye safety hazards. The HOV/HOT lane application will require an illumination spot of sufficient size to at least encompass the cabin interior of a typical sized private vehicle. Such a scenario will be described next as part of the calculation process.

Table 6.1. ANSI Laser Device Classification[1]

Class	Max Power (mW)	Logotype	Warning Label Text
I	<,= 0.39	None Required	None Required
IIa	> 0.39 to 1.0	None Required (Exposures < 1,000 s)	None Required
II	<,= 1	CAUTION	Laser Radiation - Do not stare into beam
IIIa	<,= 5	CAUTION (Irradiance < 2.5 mW/cm^2)	Laser Radiation - Do Not Stare into Beam or View Directly with Optical Instruments
		CAUTION (Irradiance >,= 2.5 mW/cm^2)	Laser Radiation - Avoid Direct Eye Exposure
IIIb	<,= 500	DANGER	Laser Radiation - Avoid Direct Exposure to Beam
IV	> 500	DANGER	Laser Radiation - Avoid Eye or Skin Exposure to Beam

6.2 SAFETY CALCULATIONS FOR PULSED IR LASER SOURCES

There are two steps to assess eye safety hazard. The first step is to determine the Maximum Permissible Exposure (MPE) in terms of energy or power per unit surface area, referred to as "Radiant Exposure" and "Irradiance" respectively. The second step is to then calculate the Nominal Hazard Distance (*NOHD*) from the source where the MPE holds true (Figure 6.1). This is affected by beam divergence which affects the Radiant Exposure (Joules / cm^2·sr^{-1}). The calculations herein assumed direct unhindered viewing by the vehicle occupants of the laser point source positioned near the roadway.

[1] There is also a 2nd, international standard, IEC 60825-1, published in 2007 which includes a 3R class (105 mW).

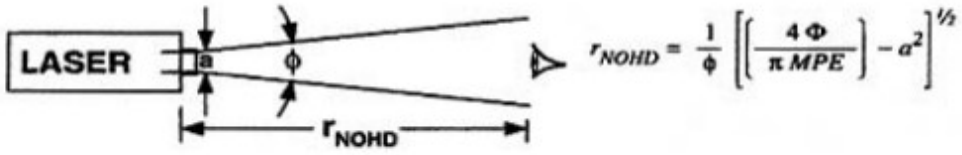

Figure 6.1. Nominal Hazard Distance (NOHD) estimate for direct viewing of a point-source laser.

6.2.1 Step 1:MPE for Continuous Wave IR lasers

The calculations begin with an HOV/HOT lane IR illuminator deployment scenario as shown in Figure 6.2. It is assumed that the vehicle is traveling at a speed of 25 mph (36.7 ft./sec.). Such a speed is of course are infrequently this low but arguably serves as a 'worse case' scenario in terms of human eye exposure time. The desired project spot size onto windshields is assumed to be a 2 meter radius (6 ½ feet) which approximates the width of the lane. The area of the circular spot is therefore equal to $\pi \cdot 200^2 = 125{,}707\ cm^2$. The pulsed laser, for example a Wedge XB series from RPMC Lasers (Missouri, USA) has the following characteristics (they are available with different output energy and powered pulse specifications from a few millijoules up to several joules in a single pulse):

Given:

$\lambda_{low\text{-}band}$= 1064nm, Energy per pulse = 4 mJ.

Approximate pulse width, $PW_{low\text{-}band} \approxeq$ 1.5 nanosec

Pulse frequency, $PF_{low\text{-}band}$= 2 KHz

Minimum speed of vehicle = 25 mph = 36.7 ft./sec.

Desired projected spot size perpendicular to windscreen = $\pi \cdot 200^2 = 125{,}707\ cm^2$

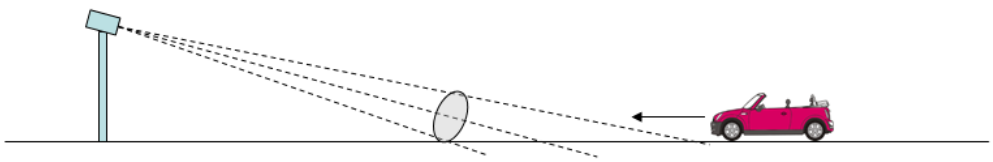

Figure 6.2. Illuminator deployment scenario above the oncoming traffic HOV/HOT lane

It is useful to compare the MPE calculation for a continuous wave laser, with an assumed maximum exposure time range of 50 x 10^{-6} < T_{max} < 10 seconds, $MPE = 9.0 \cdot C_c \cdot t^{0.75}$ x 10^{-3} J/cm^2. Since C_c= 1.0 for $\lambda_{lower\ band}$= 1064nm, and assume t=2 seconds, the MPE = 5.35 mJ/cm^2. The total illuminator energy required to achieve this level of radiant exposure equates to $125{,}707\ cm^2 \times 5.35\ \mathrm{mJ/cm^2}$, or 672.5 Joules. Or, converted to Watts (J/sec.): 672/2 seconds = 336 Watt continuous wave laser. Actually an exposure time of 2 seconds is a somewhat conservative estimate depending on the location of the illuminator and the desired projected illumination spot geometry. This is elucidated further in the next step.

6.2.2 Nominal Hazard Distance for Continuous Wave Illuminator

The NOHD calculation will assume the exit beam aperture, *a*, is small (~ 1 cm). To calculate an optical beam divergence ϕ, suppose the position of the illuminator source is placed 22 feet (6.7 meters) overhead aimed 60 feet (18.2 m) upstream of oncoming traffic in the lane, and we want to achieve the aforementioned 2 meter radial spot projection. Then $\phi = 2 \cdot atan^{-1}\left(\frac{1\ meter}{\sqrt{18.2^2 + 6.7^2}}\right) = 5.88° = 0.102\ rad$. As previously noted an exposure time of 2 seconds is a conservative estimate given the desired illumination spot size. If the vehicle is traveling 25 MPH (36.7 ft./sec), which could be considered a very low speed in the HOV/HOT lane, the windshield will be within the spot cone volume for 20/37 = 0.54 seconds. For the power $\boldsymbol{\Phi}$ = MPE:

$$r_{NOHD} = \frac{1}{0.102} \cdot \left[\left[\frac{4 \cdot 5.35}{\Pi \cdot 5.35}\right] - 1.0^2\right]^{1/2} = 5.1\ cm \qquad (6.1)$$

Therefore, because the divergence angle is so large, the driver is well beyond the nominal hazard distance and therefore well below the MPE.

6.2.3 Step 1: MPE for Pulsed IR Lasers

The Pulse laser MPE calculation is more involved because human tissue absorption effects must be considered. Generally, three calculations are performed, whereby the minimum result of the three determines the MPE. The first, MPE_1, states that no single pulse in a chain of pulses exceeds the MPE. The second, MPE_2, states that the average power from a group of pulses over a time period *T* cannot exceed the MPE within that time period *T*. And finally MPE_3, which addresses the possibility of thermal injury if a sequential group of pulses are fired at a duty period less than t_{min} is MPE_1 multiplied by a multiple pulse correction factor, C_p. Furthermore, for an IR bands under 1050nm, the largest duty period between pulses t_{min} = 18 μsec (55.55 kHz), and for IR bands less than or equal to 1400nm, t_{min} = 50 μsec (20 kHz).

To proceed, with $PW_{low\text{-}band} = 1.5 \times 10^{-9}$ seconds, and with $\lambda_{low\text{-}band}$= 1064nm, the Q-switched Solid State lasers can typically provide a pulse train duty cycle of 2 KHz (for example, Bright Solutions, Inc.). Keeping with the exposure time constraints mentioned previously to no more than 1 millisecond to minimize

blurring in this scenario [8], and with the maximum sensor frame rate of 30 fps, then implies that the HOT/HOV lane occupants will be exposed to a maximum of 2 pulses x 30 Hz = 60 pulses (assuming a data collection period of 1 second which is actually quite long assuming an accurate 'trip wire' triggers the start data collection when the vehicle passes into the data collection viewing volume containing the vehicle. In addition, an external TTL strobe and TTL trigger signal must be supplied to the laser control modules).

MPE_1: $MPE = 5.0 \cdot C_c \cdot t^{0.75} \times 10^{-3}$ J/cm^2 for 1 x $10^{-9} < T_{max} <$ 50 x 10^{-6} seconds; C_c=1.0

$$MPE = 5.0 \cdot 1.0 \cdot (1.5 \times 10^{-9})^{0.75} \times 10^{-3} = 1 \text{ x } 10^{-7} \text{ m J/cm}^2$$

MPE_2: $MPE = 5.0 \cdot 1.0 \cdot (1.0)^{0.75} \times 10^{-3}/60$ pulses = 0.83 m J/cm^2

MPE_3: $MPE = MPE_1 \cdot C_p = MPE_1 \cdot n^{-0.25} = 1 \text{ x } 10^{-7} \cdot 60^{-0.25} = 3.59 \text{ x } 10^{-8}$ m J/cm^2

Employing the aforementioned minimum MPE criteria, then MPE_3 is the smallest, which presents the limiting MPE of only 3.59 x 10^{-8} m J/cm^2. However, because the duty cycle period for any group of pulses exceeds t_{min} , MPE_1 is used for relevant calculations. The Nominal Hazard distance for the MPE is still 5.1 cm ($\Phi = MPE_3$).

The second "high band" pulsed IR laser is available at $\lambda_{low\text{-}band}$= 1534nm is absorbed by skin as well as the eye tissue in front of the retina. From table 5.a, the CW value for a maximum exposure period, 1 x $10^{-9} \leqq T_{max} <$ 10 seconds, MPE = 1.0 J/cm^2 -- a very high number. Considering the pulsed $\lambda_{low\text{-}band}$= 1534nm Wedge XB laser releases 1 mJ of energy in under 1.5 x 10^{-9} seconds, this equates to a concentrated power output equivalent of 666.6 kW. Note that the energy output of the 1064nm laser is 4 mJ, with a similar pulse width, producing an average power equivalent 2.66 MW (manufactured spec of peak power up to 4 MW).

6.2.4 Nominal Hazard Distance for Pulsed IR Laser Illuminators

With the candidate lasers using the desired projected spot size on the vehicle, the radiant exposure risk to a driver's eyes can be evaluated in the second step. Of course, if the light energy is attenuated through the vehicle glass the risk is further reduced -- perhaps significantly so. However, we still assume a 'worse case' scenario: for example a side passenger window is rolled down while the vehicle is moving slowly through the data collection spot area. Recalling that $\phi = 5.88^\circ = 0.102\ rad.$ to achieve a 2 meter spot radius, the surface area estimate is therefore 125,707 cm^2. Then radiant exposure level for the 1064 nm laser pulsed laser is 4 mJ/125,707 cm^2 = 3.182 x 10^{-5} mJ/cm^2. This is 3.182 x 10^{-5}/1 x 10^{-7} = 318.2 times the MPE, thus

$$r_{NOHD-1064\,nm} = \frac{1}{0.102} \cdot \left[\left[\frac{4 \cdot 3.182 \times 10^{-5}}{\Pi \cdot 1 \times 10^{-7}} \right] - 1.0^2 \right]^{1/2} = 196.9\ cm \approx 2\ meters \qquad (6.2)$$

Since the vehicle distance is greater than Nominal Hazard Distance of 2 meters, there is minimal eye safety hazard risk since the exposure would be below the MPE (in laser safety parlance, no 'safety barrier' would be required).

For the $\lambda_{low\text{-}band}$= 1534nm laser, the radiant exposure level is 1 mJ/125,707 = 8.0 x 10^{-6} mJ/cm^2: well below the MPE to begin with.

6.3 POWER IRRADIANCE

The Power Irradiance, *P*, for a given exit pulse of approximately 1.5 nanoseconds of light energy for each of the lasers using the aforementioned spot diameter, can thus be estimated:

$P_{1534\,nn} = \frac{666.6\ kW}{125{,}707}$=5.3 W/cm^2

$P_{1067\,nn} = \frac{2{,}667\ kW}{125{,}707}$=21.2 W/cm^2

6.4 INCANDESCENT AND LED IRRADIANCE CHARACTERISTICS

It is also of interest to estimate IR spectral power characteristics of the incandescent IR illuminator, as well as the sun – another IR illumination source-- to provide further context to eye safety risk and illumination power. The table below, separates the spectral power irradiance of the sun into bands that are relevant to the TBI, as well as other common IR sensor IR illuminator ranges.

Table 6.2. Sunlight IR Irradiance Levels

IR band description	IR wavelength range	Power flux (mW/cm^2)
Total IR	700 nm - 2500 nm	43.17
SWIR TBI lower band	900 nm - 1400 nm	17.45
SWIR TBI upper band	1400 nm - 1700 nm	4.95
IR band car windshield transition zone [7], [11]	800 nm - 850 nm	4.38

The spectral power output characteristics of the TBI incandescent IR spot light illuminator could not be found. As an approximation suppose we base the calculations from a typical incandescent bulb [23]. A 100 W bulb outputs between 35 to 40 Watts in the NIR spectrum. Since the illuminator halogen bulb is listed at 220 W, we will assume a maximum of 85W of NIR light (black body radiation spectral model at 3200K), emanating from a 30 degree/15 degree major/minor 'elliptical cone'. For the incandescent TBI

Derwent IR illuminator, at 2.5 meters, an estimate of the total possible irradiation area is $A = \Pi \cdot 2.5^2 \cdot tan(30/2) \cdot tan(15/2) \cong 0.69\, meters^2$ giving the IR light power irradiance of approximately 85W/0.69 m^2 or 12.3mW/cm^2: 38% of the full sun irradiance. However, if we consider the cut filter range starting at 900nm, the TBI SWIR lower and upper band irradiance is approximated to be 31W/0.69 $m^2 \cong$ 4.34 mW/cm^2 and 15W/0.69 $m^2 \cong$ 2.17 mW/cm^2 respectively. This is ideal conditions and assume no loss in efficiency in transmitting all the IR light through the reflector and lens. The illumination area would need to be increased to cover more of the vehicle, thereby reducing the irradiance even further. Referring to Table 5.3 calculations for the active IR illuminator setup to achieve most of the successful detections result in lower band irradiance of 22.39 mW/cm^2 and an upper band irradiance of 9.88 mW/cm^2.

To conclude incandescent illuminators do not appear to impose serious eye hazards especially with such large dispersion angles. However, to achieve elevated energy requirements may become an intractable problem to power and deploy such a system.

CHAPTER 7: CONCLUSIONS

First and foremost, one can conclude that it is possible to penetrate vehicle glass to detect the presence of human occupants. We demonstrated that a computationally efficient algorithm allows adaptation for varied conditions while allowing simple quantitative comparison of such conditions on the TBI skin detection performance. Furthermore, the SWIR detection was successful in cases where glare and blooming in the visible band image confounded ability to visibly identify subjects within the vehicle cabin. Second, variability in model and manufacturer optical characteristics of vehicle glass were apparent even with the small set of sample cases observed in these experiments. We were also somewhat surprised that bright sunlit conditions do not necessarily contribute to improved detection results. This was due to other reflective glare and blooming on the vehicle window surfaces, which could not be removed in the lower IR band. Perhaps one recommendation therefore for future deployment of the TBI sensing technology is that the sensor should intentionally be positioned to capture vehicle positions out of direct sunlight if possible; for example, beneath overpasses where the sun would tend to be blocked.

The study suggests that very high illumination power on the order of 30 KW may be required for high-speed vehicle detection. This may be impractical to achieve with continuous illumination technology. Pulsed IR lasers can be considered, paying attention to ensure there are no eye safety hazard risks to motorists. As mentioned in Chapter CHAPTER 5: , it is important to note that the capabilities of the SWIR sensing technologies have improved dramatically over the past 10 years. For example, the replacement SWIR image sensor having the same InGaAs FPA resolution and pixel pitch is over *40 times* more sensitive than the current sensors. Therefore, significantly larger signal-to-noise ratios would be achieved for the same experimental conditions. As a practical deployment matter, more recent SWIR sensors also implement common digital interface standards, such as Camera Link and GigE, for precise timing control and acquisition. This provides interchangeability between camera sensor and data acquisition hardware and more flexibility in locating and powering sensor and processing hardware than the TBI.

Moving forward, another recommendation for future development is to utilize a low-cost NIR camera closer to the 'transition band' ($800nm < \lambda < 850nm$) of windshields, to provide similar data to the lower band IR sensor since human skin is also reflected in this band. In addition, other studies indicate that some of the glare effects are reduced within this spectral range. From another general observation of the experiments, the upper band IR channel appeared to have slightly better performance than the lower band, even for cases where segmentation and detection of the occupants could not be achieved. In addition, potentially there is low eye hazard risk associated with artificial illumination for the SWIR upper band spectrum ($1400\ nm < \lambda < 1700nm$) compared with the lower band spectrum ($900nm < \lambda < 1400\ nm$). Therefore, the upper band alone could serve as an assistive tool for lane enforcement activities, by simply identifying subject face silhouettes.

Finally, this study did not evaluate automated methods for human occupancy detection and counting. However, there are many techniques to build facial features for machine learning human facial recognition, which have already been demonstrated to be fairly robust for this application. All such

machine learning techniques require extensive accurate training data that should contain a large set of varied operational scenarios to build robust classifiers. Nevertheless, good performance using any of these methods with the TBI relies fundamentally on robust human subject segmentation from within the vehicle, which was the main focus of this study. Notwithstanding, even without automated occupancy detection and counting, if robust segmentation can be achieved, the resulting output would also serve as a valuable tool for law enforcement officers to remotely monitor HOV locations and quickly identify and isolate violators.

REFERENCES

[1] J. Kwon and P. Varaiya, "Effectiveness of California's High Occupancy Vehicle (HOV) System," *Transportation Research Part C,* vol. 18, pp. 98-115, 2008.

[2] K. F. Tumbull, "Evolution of High-Occupancy Vehicle Facilities: Maximizing Efficiency and Effectiveness," *TR News (Special HOV Issue),* May-June 2001, pp. 6-11, 2001.

[3] X. J. Cao, Z. Xu and A. Y. Huang, "Safety Benefits of Converting HOV Lanes to HOT Lanes: Case Study of the I-394 MnPASS," *ITE Journal,* vol. 82, pp. 32-37, 2012.

[4] I. R. Feldman, P. A. Moosie and B. E. Patno, "Mobile enforcement reader," U.S. Patent No. US7382275, 06/03/2008, U. S. Patent and Trademark Office, Washington D.C., 2008.

[5] TTI, "Technology Approaches to HOV Occupancy Declaration and Verification: State-of-the-Practice Review ," unpublished, April 8, 2014, pp. 1-16, 2014.

[6] T. Harlow, "State Patrol, MnDOT partnering to crack down on carpool lane cheaters," *StarTribune,* August 17, 2016, 2016.

[7] W. Daley *et al*, "Detection of vehicle occupants in HOV lanes: Exploration of image sensing for detection of vehicle occupants," in *IS&T/SPIE Electronic Imaging Video Surveillance and Transportation Imaging Applications,* Burlingame, California, 2013, pp. 86630S-15.

[8] I. Pavlidis *et al*, "Automatic detection of vehicle occupants: the imaging problem and its solution," *Machine Vision and Applications, vol. 11, no. 6,* pp. 313-320, 2000.

[9] M. Bertozzi *et al*, "Pedestrian detection in poor visibility conditions: Would SWIR help?" in *Image Analysis and Processing - ICAP 2013,* pp. 229-238, Naples, Italy, 2013.

[10] X. Hao *et al*, "A near-infrared imaging method for capturing the interior of a vehicle through windshield," in *Image Analysis & Interpretation (SSIAI), 2010 IEEE Southwest Symposium,* pp. 109-112, Austin, TX, USA, 2010,

[11] X. Hao *et al*, "Occupant Detection through Near-Infrared Imaging," *Tamkang Journal of Science and Engineering,* vol. 14, pp. 275-283, 2011.

[12] W. Daley *et al*, "Sensing system development for HOV (high occupancy vehicle) lane monitoring," Georgia Transportation Institute, Tech. Rep. RP 07-26, Atlanta, Georgia,. 2011.

[13] M. Rosen, "System for Automated Detection of Mobile Phone Usage," U.S. Patent No. US20120040650 A1, 02/16/2012, U. S. Patent and Trademark Office, Washington D.C., 2012.

[14] Y. Zhang, B. Xu, L. K. Mestha and G. Pennington, "Systems and methods for detecting cell phone usage by a vehicle operator," U.S. Patent No. US9165201 B2, 10/20/2015, U. S. Patent and Trademark Office, Washington D.C., 2015.

[15] E. N. Dalal, P. Paul, L. K. MESTHA and A. S. Islam, "Vehicle occupancy detection via single band infrared imaging," U.S. Patent No. US8811664 B2, 08/19/2014, U. S. Patent and Trademark Office, Washington D.C., 2014.

[16] I. Pavlidis, V. Morellas and N. Papanikolopoulos, "A Vehicle Occupant Counting System Based on Near-Infrared Phenomenology and Fuzzy Neural Classification," *IEEE Transactions on Intelligent Transportation Systems,* vol. 1, pp. 72-85, 2000.

[17] E. Holec *et al*, "Monitoring and use of HOV and HOT lanes," Tech. Rep. CTS-13-07, January 2013, ITS Institute, Center for Transportation Studies, University of Minnesota, Minneapolis, Minnesota, 2013.

[18] C. Chan *et al*, "Implementation and evaluation of automated vehicle occupancy verification," California Path Program, Tech. Rep. UCB-ITS-PPR-2011-04, May 2011, Institute of Transportation Studies, University of California, Berkeley, Berkely, California, 2011.

[19] H. Bay, T. Tuytelaars and L. Van Gool, "SURF: Speeded up robust features," pp. 404-417, in *European Conference on Computer Vision,* Graz, Austria, 2006.

[20] K. Zuiderveld, "Contrast limited adaptive histogram equalization," in *Graphics Gems IV*, P. Heckbert, Ed. Academic Press, San Diego, CA, 1994.

[21] M. W. Burke, *Image Acquisition: Handbook of Machine Vision Engineering (Vol 1).* New York, NY: Springer Science & Business Media, 2012.

[22] Anonymous, *American National Standard for Safe use of Lasers.* Orlando, Florida: Laser Institute of America, 2007.

[23] Goldwasser, S. M., *Sam's Laser FAQ, A Practical Guide for Experimenters and Hobbyests*. Available: http://www.repairfaq.org/sam/lasersam.htm., accessed: 03/05/2014